Investigations of the Semi-Insulating $LiIn_{1-x}Ga_xSe_2$ Solid Solution for Neutron Detection

By

Brenden Wayne Wiggins

Dissertation
Submitted to the Faculty of the
Graduate School of Vanderbilt University
in partial fulfillment of the requirements
for the degree of

DOCTOR OF PHILOSOPHY
in

Physics
August, 2016
Nashville, Tennessee

Approved:

Keivan Stassun, Ph.D.

Arnold Burger, Ph.D.

Ashley Stowe, M.B.A., Ph.D.

Kalman Varga, Ph.D.

Norman Tolk, Ph.D.

To my supportive family

ACKNOWLEDGEMENTS

First, I would like to thank my supportive family for their love, support and wisdom. Secondly, I would like to thank my advisor and committee members for their time, patience and for generating an opportunity for me to do the science that I find interesting. Lastly, I would like to thank my mentors for taking the time to listen to me and provide advice when it was needed.

TABLE OF CONTENTS

LIST OF TABLES

LIST OF FIGURES

CHAPTER I

INTRODUCTION

Neutron Detection Technology

The neutron was discovered by James Chadwick in 1932. In his scattering apparatus, he deduced the identity of an unknown penetrating, electrically neutral product from alpha particle bombardment on a Beryllium target. [1] The neutrons discovery brought forth new technology that had the ability to detect these particles. Because neutrons have no intrinsic charge, we must detect neutrons indirectly via nuclear reactions. A commonly utilized nuclear process is the neutron activation process: when a neutron is captured into the nucleus, this makes the nucleus heavier and achieves an excited state; upon de-excitation, the nucleus undergoes fission and decays into products which can be observed in experimental procedures. This process is governed by conservation laws i.e. conservation of energy, momentum, mass and charge. In the early detection apparatuses, Boron tri-fluoride (BF_3) gas filled tubes were utilized for the application of neutron counting. [2] This device used the neutron activation process of ^{10}B, which has a thermal neutron cross-section of 3,835 barns, to detect these particles indirectly. The concept of cross-section derives from the probability of free neutron interaction; in this case, the interaction is neutron capture. Cross-sections are measured in the units of barns (1 barn = $10^{-24}cm^2$). Thermal neutrons are characterized by neutrons that have energy of 0.025 eV. The neutron-^{10}B reaction has two possible events; these events are conveniently defined as event (I) and (II) in figure 1. Upon de-excitation of the boron nucleus, it can undergo fission producing an energetic ${}^{7}_{3}Li$ atom and an alpha particle ${}^{4}_{2}\alpha$ or an excited energetic ${}^{7}_{3}Li$ atom and an alpha particle ${}^{4}_{2}\alpha$. Here, only a small fraction of 6% branch to event II; however, both events produce products that can ionize the gas. The electrons generated can then be accelerated

with a bias (potential difference) towards a collector wire and analyzed with pulse height spectra analysis (signal processing). However, exposure of the gas to moisture generates health concerns. The gas is toxic and its reaction with water (H_2O) yields acidic products, making this device difficult to handle with leaks in humid environments. Other neutron gas detectors currently used are Helium-3 (^{3}He) proportional counters. With its high cross-section for the thermal neutrons, measured to be 5,333 barns, ^{3}He is an attractive standard for thermal neutron detection. ^{3}He is a noble gas and is also ideally applied to high pressure gas neutron sensors. This device utilizes the neutron-^{3}He reaction, defined by event (III) in figure 1, which produces an energetic proton ${}_1^3H$ and a triton ${}_1^3H$, then ionizes the gas; from this induced event, the electrons move towards the collector wire induced by an applied bias and becomes collected for signal processing. However, dense gas proportional counters come with their own set of problems including high bias operation, transportation difficulties for tubes with large geometries and sensitivity to noise generation.

$$ {}_5^{10}\boldsymbol{B} + {}_0^1\boldsymbol{n} \rightarrow {}_5^{11}\boldsymbol{B}^* \rightarrow {}_3^7\boldsymbol{Li}(\mathbf{1.015}\boldsymbol{MeV}) + {}_2^4\boldsymbol{\alpha}\,(\mathbf{1.777}\boldsymbol{MeV}) \qquad (\boldsymbol{I}) $$

$$ {}_5^{10}\boldsymbol{B} + {}_0^1\boldsymbol{n} \rightarrow {}_5^{11}\boldsymbol{B}^* \rightarrow {}_3^7\boldsymbol{Li}^*(\mathbf{.84}\boldsymbol{MeV}) + {}_2^4\boldsymbol{\alpha}(\mathbf{1.47}\boldsymbol{MeV}) \qquad (\boldsymbol{II}) $$

$$ {}_2^3\boldsymbol{He} + {}_0^1\boldsymbol{n} \rightarrow {}_2^4\boldsymbol{He}^* \rightarrow {}_1^3\boldsymbol{H}(\mathbf{573}\boldsymbol{keV}) + {}_1^1\boldsymbol{H}(\mathbf{191}\boldsymbol{keV}) \qquad (\boldsymbol{III}) $$

Figure 1 Common converter isotope reactions used in high pressure gas neutron counters.

Navigating away from traditional gas detectors, in the subset of alternative systems, glass converter compounds, halide converter compounds, and converter film coupled devices have all been investigated. Specifically addressing the scintillator subset of alternative systems, these systems also have the ability to convert incident thermal neutrons into ionizing radiation;

however, this event induces scintillation, assisted by the activator, in the host material. In the scintillator device subset, efficient luminescence determines the applicability of the device. This makes light quenching play an important role in determining practical use of a scintillator device. Quenching is the mechanism that represents the loss in the conversion to light in the host material; this makes size, composition and activator concentration parameters to optimize. [2] National focus on these alternative systems has led to the development of high performing scintillator materials applicable to thermal neutron applications; these include compounds such as $Cs_2LiYCl_6:Ce^{3+}$, $Li_3YCl_6:Ce^{3+}$, $LiCaAlF_6:Ce^{3+}$, $LiI:Eu^{2+}$. [2,3,4] However, due to the reactivity of these alkali metals, applying the alkali-halide compounds materials to practical applications has posed challenges in either handling or maintaining material uniformity. Considering the issues generated from the alkali-halide compounds, $ZnS:Ag^{2+}$ mixed with converter materials (^{6}LiF or $^{10}B_2O_3$) has also developed into a practical alternative scintillator system. [5] This scintillator system is commercially available and eliminates the difficulties associated with the alkali-halide compounds; however, due to the nature of the heterogeneous mixture, high light yield values are difficult to achieve due to light scattering. Lastly, within the scintillator subset, lithium activated glass can also produce considerable reliability in thermal neutron energy ranges; in the current market, these materials can cover large areas of interest at low cost. [2] One of the advantages of using solid converter systems is that the neutron can be capture in a relatively small volume, due to the converter density in the solid phase, making solid converter systems ideal for small volume device imaging arrays.

For coupled devices, some current thermal neutron detectors utilize a reactive film, such as ^{6}LiF or $^{10}B_2O_3$. Host materials in this subset include bulk semi-conductors, such as Silicon (Si) and

Gallium Arsenide (GaAs), which have deposited converter films. However, variations in converter film thickness can severely impact the efficiency of the device. [6,7,8,9] Thick reactive films can behave as a shield and absorb the neutron reaction products reducing the efficiency of the device. However thin reactive films can reduce the amount of neutrons converted also reducing the efficiency of the device. This fact makes the reactive film thickness a parameter to optimize with coupled devices. [8,9] The main drawback to solid-state alternative materials is there gamma sensitivity, making the detection of neutrons difficult in the presence of gamma radiation. While pulse shape discrimination (PSD) can partially mitigate this effect, it is computationally expensive and requires large amounts of power.

Gamma Interactions in Matter

There are three main gamma interactions in crystalline media: Photon absorption, Compton scattering and pair-production; here, each interaction probability is dependent on the crystal system and incident energy. [2]

In the photon absorption process, the interaction takes place within atomic constituents; the incident energy is used to ionize the atomic constituents and generate a photoelectron and a hole. Here, the energy of the photoelectron is dependent on the binding energy E_b and the incident gamma ray energy hv. The analytic expression is given below:

$$E_{e^-} = hv - E_b$$

In time, the hole can be filled by an electron from a higher atomic energy level; these induced radiative transitions that are allowed produce characteristic X-rays. Alternately, the residual

energy can also be re-absorbed through electron rearrangement of surrounding atomic electrons; these induced non-radiative transitions are called Auger processes. Generally, the photon absorption process is dominant in low energy regimes; the cross section for the photoelectric effect depends strongly on the atomic number and the incident photon energy.

$$\sigma_{absorption}\ \alpha\ \frac{Z^5}{E_{photon}{}^{3.5}}$$

Here, Z is defined as the atomic number and E_{photon} is the incident photon energy.

Compton scattering is a process that describes an elastic collision between a photon and an electron which yields a recoil electron and scattered photon; here, the transfer of energy between the two particles depends on the scattering angle θ.

$$hv' = \frac{hv}{1 + \left(\frac{hv}{mc^2}\right)(1 - cos\theta)}\ ,\ E_{e^-} = hv - hv'$$

Here, hv is the incident photon energy, hv' is the scattered photon energy, mc^2 is the rest mass energy of the electron and E_{e^-} is the energy the electron.

Pair production is a process that takes place in the coulomb field of the nucleus; the incident photon energy is used to produce a positron-electron pair. For the pair production process, the incident energy must be greater than twice the value of the rest mass energy of the electron.

$$E_{photon} > 2mc^2\ ,\ E_{e^-} + E_{e^+} = E_{photon} - 2mc^2$$

Here, E_{e^+} is the energy of the positron. Additionally, the positron can annihilate through the interaction with electrons, resulting in annihilation photons.

Scintillation Characteristics

Generally, the scintillating characteristics of interest are the stability of its response function, its capability to operate in radiation background environments and the time requirement to count the event. These technical characteristics are defined as radiation hardness, light yield and decay time respectively. [2]

Light yield is a measure of the scintillator crystal response to incident radiation; two known quantities that characterize the crystals response to incident radiation are defined as absolute light yield and relative light yield. The relative light yield is a ratio of the total number of emitted photons detected by the photocathode in the photomultiplier tube (PMT) to the energy deposited in the scintillator crystal by ionizing radiation. Here, the number of emitted photons is extracted by the photoelectron yield using the quantum efficiency of the device. The quantum efficiency Q_{PE} is defined below:

$$Q_{PE} = \frac{N_{pe}}{N_{ph}}$$

Here, the N_{pe} term represents the number of photo-electrons and the N_{ph} term represents the incident photons. Absolute light yield is the ratio of the total number of photons emitted to the energy deposited in a scintillator. Due to this fact, the absolute light yield is a difficult experimental quantity; this quantity depends on numerous experimental parameters: the type of light reflector, geometrical considerations, optical coupling to the PMT and the quantum efficiency of the photocathode. Due to the fact that there are errors associated with each parameter, these observations make the absolute light yield difficult to obtain.

The decay time is used to characterize the prompt scintillation yield temporally; this quantity describes the time evolution of the number of scintillation photons in a single scintillation event. For PSD applications, this quantity is utilized as an additional parameter to separate gamma events from neutron events. Generally, the decay time is usually calculated through fitting the experimental signal traces to a weighted sum of exponential decay functions. The general expression is given below:

$$I(t) = \sum_{i}^{N} I_i \, e^{\frac{t}{\tau_i}}$$

Elements of Density Functional Theory

In mathematics, a functional is a function that takes another function as its argument. Density functional theory (DFT) derives from the fact that terms in the system's Hamiltonian can be expressed as functionals of the density. For many periodic condensed matter systems, we are mainly interested in the electrons in the system; this is because electrons are much less massive than nuclei, allowing the electrons to respond to forces much faster than the nuclei. In this case, we can use the Born-Oppenhemier approximation which states that the wave function of the entire system, which includes both electrons and nuclei, can be separated into an electron component and a nuclei component; this allows us to concentrate on the electronic wave function. This approximation is used for all calculations in this dissertation.

In principle, understanding quantum mechanical systems begins with solving the time independent Schrödinger equation to obtain the ground state wave function Ψ for the system:

$$H\Psi = E\Psi$$

Here, H is the system's Hamiltonian and E is the energy. Unfortunately, for a system with a large number of electrons, a general solution can be complex due to the multiple electron-electron interactions in the many-electron system. Traditionally, the Hartree method was utilized to obtain the many-body wave-function Ψ; however, the Hartree method approximated the many-electron wave function as a product of N single electron wave functions. Generally, the product of N single electron wave functions assumes that the electrons are independent of each other; additionally, this general approach does not incorporate the anti-symmetrization of the wave function by neglecting particle exchange. The Hartee method wave-function is given below; in the equation, N represents the number of electrons in the system.

$$\Psi(r_1, r_2 \dots r_N) = \phi_1(r_1)\phi_2(r_2) \dots \phi_N(r_N)$$

Progressively moving forward, the Hartree-Fock method provided an improvement to the original Hartree method by utilizing an anti-symmetrized product of single-electron wave functions. The difference between the Hartree method and the Hartee-Fock method is the exchange energy; here, the exchange energy is the contribution to the coulomb energy through spatial separation of electrons via spin dependence. In the Hartee-Fock method, the general form of the many-body wave-function Ψ can be express by the evaluation of the Slater determinant given below:

$$\Psi(r_1, r_2, \dots r_N) = \frac{1}{\sqrt{N!}} \begin{bmatrix} \phi_1(r_1) & \phi_1(r_2) & \cdots & \phi_1(r_N) \\ & \vdots & \ddots & \vdots \\ \phi_N(r_1) & \phi_N(r_2) & \cdots & \phi_N(r_N) \end{bmatrix}$$

However, this method exhibits statistical variation and neglects correlation contributions. The difference between the total coulomb energy of the electronic system and the Hartree-Fock energy is the correlation energy.

In consideration of the theoretical framework, once the many-body wave-function is known explicitly, the density can be obtained through integration.

$$n(\vec{r}) = N \int \dots \int \left| \Psi(r_1, r_2, \dots r_N) \right|^2 dr_1 \dots dr_N$$

However, the traditional approach can become difficult as the number of electrons N increases. The concept in DFT is that one does not need to calculate the many-body wave-function Ψ; as a replacement for the many-body wave function, the electron density $n(\vec{r})$ is sufficient. The rationalization for this concept derives from the Hohenberg-Kohn (HK) theorems and treatment of the electrons in a system as a non-interacting electron gas. From this viewpoint, the total energy functional of a system of electrons moving under the influence of an external potential is a unique functional of the electron density. [10] This concept converts a problem with N electrons, which has 3N spatial coordinates, to one with just the three spatial coordinates; this drastically reduces computational requirements. Additionally, the ground state energy can be obtained through variational methods; this means that the density that minimizes the total energy functional is the single particle ground state density.

Following the HK theorems, the Kohn-Sham (KS) formulation constructed a total-energy functional. The Kohn-Sham total energy functional is defined below:

$$E[\phi_i] = 2\sum_i \int \phi_i \left[\frac{-h^2}{2m}\right] \nabla^2 \phi_i d^3r + \int V_{ion}(r) n(r) d^3r + \frac{e^2}{2} \int \frac{n(r)n(r')}{|r - r'|} d^3r d^3r'$$

$$+ E_{xc}[n(r)] + \sum_{ij} \frac{Z_i Z_j}{|R_i - R_j|}$$

Here, moving from left to right, ϕ_i represents occupied electronic states, the first term represents the kinetic energy, the second term represents the electron-ion interaction, the third term

represents the electron-electron interaction, the fourth term represents the exchange-correlation energy contribution and the last term represents the ion-ion interaction. Naturally, the electron density $n(\boldsymbol{r})$ is defined below as:

$$n(r) = 2\sum_{i}^{N} \left|\phi_i(r)\right|^2$$

Complementary to this, the Kohn-Sham (KS) formulation also constructed a procedure that replaced the many-electron problem by an equivalent set of self-consistent one-electron equations; here, each independent electron is viewed as moving in an effective potential representative of the system. The Kohn-Sham equation is defined below:

$$\left[\frac{-h^2}{2m}\nabla^2 + V_{ion}(r) + V_H(r) + V_{XC}(r)\right]\phi_i(r) = \varepsilon_i\phi_i(r)$$

Where the ϕ_i is the wave function of the electronic state i, ε_i is the Kohn-Sham eigenvalue, V_H is the Hartree potential of the electrons, V_{ion} is the ion potential and V_{XC} is the exchange-correlation potential. Here, both the Hartree potential and exchange-correlation potential respectively are defined below as:

$$V_H(r) = e^2\int \frac{n(r')}{|r-r'|}d^3r' \, , V_{XC}(r) = \frac{\delta E_{xc}[n(r)]}{\delta n(r)}$$

Notably, while the KS formulation makes the Schrödinger equation simpler to solve, through reducing the electron interaction complexities, the generated eigenstates of the KS formulation are not eigenstates of the real system; these calculated eigenstates are known as Kohn-Sham orbitals. This consequence comes directly from the assumption that the system behaves as a non-interacting gas. In order to maintain vitality, the KS formulation constrains the density calculated from the KS orbitals to match the actual system's density. [11]

Approaching the $V_{ion}(r)$ term, this task is generally handled by the pseudo-potential approximation. Within the literature, the pseudo-potential approximation has been viewed as a complementary component to computational endeavors. [12-16] The pseudo-potential method groups the electrons in atoms/ions into two subsets, the core electrons and valence electrons. In this method, the ion-valence interactions determine the physical properties of the system while the core electrons play a passive role; due to this assumption, the core electrons are removed and the strong ionic potential is replaced with a weaker potential called pseudo-potential. Together with the pseudo-potential approximation, these equations and the corresponding density constraint, this allows one to calculate system observables.

Now with the theoretical framework defined, the exchange-correlation energy represents a vital quantity to determine and possess a significant amount of uncertainty in its analytical form; for various systems, numerous parameterizations exist for the exchange-correlation energy. The most basic approach to describe the exchange-correlation energy uses the local density approximation (LDA). [17,18] Taking advantage of the electron gas treatment, the exchange-correlation energy per electron at some point r is assumed to be equivalent to the exchange-correlation energy per electron of a homogeneous electron gas; this assumes that the exchange-correlation energy functional is purely local. With this assumption, the exchange-correlation energy functional and the derivative with respect to the density respectively reduce to the expressions below:

$$E_{xc}[n(r)] = \int \varepsilon_{xc}(r) n(r) d^3r \,, \frac{\delta E_{xc}[n(r)]}{\delta n(r)} = \frac{\delta[\,\varepsilon_{xc}(r) n(r)]}{\delta n(r)}$$

To improve the description of the exchange-correlation energy, additional parameters have also been utilized; these parameters include the gradient of the density $\nabla n(r)$ and higher order components. In this dissertation, we explore both the LDA formalism and the additional gradient

parameter formalism known as the general gradient approximation (GGA). [19-21]

To obtain the density for condensed matter systems with periodic potentials, such as single crystals, plane wave basis sets are useful. Generally, plane waves basis functions are orthogonal and form a complete set; with this knowledge, plane wave basis sets can approximate the electron density and simplify the procedure. This required condition can be mathematically written as:

$$V(r+R) = V(r)\,, R = n_1 a_1 + n_2 a_2 + n_3 a_3$$

Here, R represents a unit length translation operation, the set of $\{n_i\}$ are integers and the set of $\{a_i\}$ are the lattice vectors of the crystal. In a similar fashion, we can define a basis set of reciprocal lattice vectors $\{b_i\}$ that are orthogonal to the lattice vectors; the reciprocal vector G is determined by the basis vector set $\{b_i\}$.

$$b_1 = 2\pi \frac{a_2 \times a_3}{a_1 \cdot a_2 \times a_3}\,, b_2 = 2\pi \frac{a_3 \times a_1}{a_1 \cdot a_2 \times a_3}\,, b_3 = 2\pi \frac{a_1 \times a_2}{a_1 \cdot a_2 \times a_3}$$

Utilizing the Bloch theorem, the wave function of the electrons $\Psi_{i,k}(r)$ in the crystal can be written as a product of a wave-like part $e^{ik\cdot r}$ and a periodic part $u_{i,k}(r)$ respectively:

$$\Psi_{i,k}(r) = e^{ik\cdot r} u_{i,k}(r)\,, u_{i,k}(r+R) = u_{i,k}(r)$$

Here, k represents the wave-vector. [22] Due to symmetry, the periodic parts of the wave-function and potential can be expanded in terms of plane waves in reciprocal lattice space. These expressions are given below:

$$u_i(r) = \sum_G c_G e^{iG\cdot r}\,, V(r) = \sum_G V_G e^{iG\cdot r}$$

Conveniently, each electronic wave function can be written as a sum of plane waves; this allows one to generate a general form for the electronic wave-function. This expression is written below:

$$\Psi_{i,k}(r) = \sum_{G} c_{i,k+G} e^{i(G+k)\cdot r}$$

In practice, it is common to assign an energy cut-off $E_{cut-off}$ since one is unable to use the complete set; this constrains the function approximation to planes waves of a specified set. This condition is written below:

$$\frac{h^2}{2m}|G+k|^2 < E_{cut-off}$$

Considering the electronic states in single crystals have allowed k values, determined by the lattice parameters of the system, the Bloch theorem allows one to calculate a finite number of electronic wave functions at an infinite amount of k-values.; this element represents another major simplification to calculating a large number of electronic wave functions for single crystal systems. Using the plane wave expansion convention, the DFT problem can now be simplified through substituting the general form of the electronic wave function into the KS equation, evaluating the integrals over space and generating a secular equation to determine the KS orbitals; now the general task of determining the KS orbitals has transformed into a linear algebra problem. In the pursuit of solving these equations, the general procedure must be self-consisted; the self-consisted DFT procedure is described in figure 2.

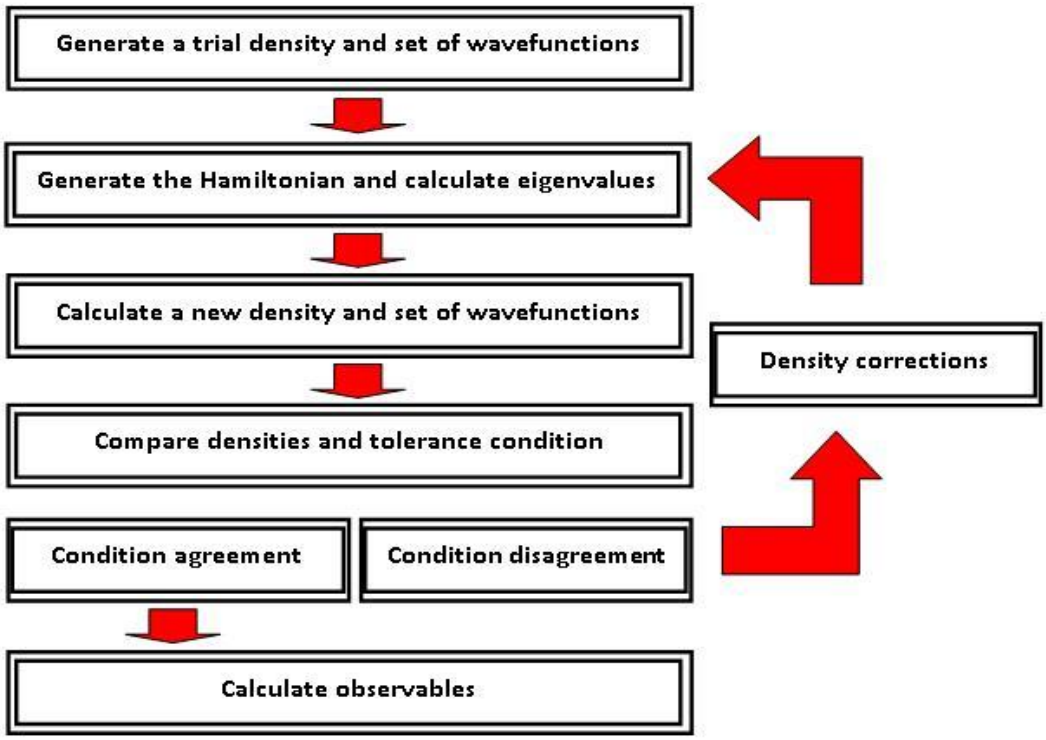

Figure 2 displays a flow chart describing the self-consistent procedure for a DFT calculation.

Elements of Crystal Growth

Crystal growth and material engineering have become complementary fields in the development of new materials with versatile optical-electrical properties. In particular, we are interested in crystalline material. Crystalline material has two subsets, single crystals and polycrystalline material. A single crystal is a solid where the arrangement of atoms is periodic, such that the structure exhibits periodic symmetry in a finite volume. Polycrystalline material is a material that is composed of small crystalline regions separated by boundaries which are classified as grain boundaries. Regarding the thermodynamics of crystal growth, the minimization of free energy dictates the crystal growth process; within the constant pressure and temperature regime, one minimizes Gibbs free energy. Gibbs free energy is the thermodynamic quantity that is

minimizes when a system achieves chemical equilibrium. The analytic expression for Gibbs free energy and its corresponding implicit differentiation is given below:

$$G = H - TS\,,\;\; \Delta G = \Delta H - T\Delta S$$

Here, H is defined as the enthalpy, T is the temperature, Δ is the differential operator and S is the entropy. Highlighting the important features, the ΔH term represents the energy change through heat absorbed or released while the $T\Delta S$ represents the energy change via state configuration; both terms can actively dictate the growth process and contribute to the available energy for solid-solution production.

Nucleation occurs through compositional fluctuations within a saturated solution; through these compositional fluctuations, material clusters can form called crystal embryos. Once formed, the stability of these spherical embryos is determined through changes in Gibbs free energy. There are two types of nucleation, homogenous and heterogeneous. To first approximation, the change in Gibbs free energy for homogenous nucleation is determined through a competitive battle between changes is bulk free energy and surface energy. The analytic expression is given below:

$$\Delta G_{homo} = \frac{4}{3}\pi r^3 \Delta G_v + \; 4\pi r^2 \gamma_{ls}$$

Here, r is the radius of the crystal embryo, ΔG_v represents the change in free energy per unit volume (bulk free energy), γ_{ls} represents the surface energy of the solid and liquid phase. Navigating through differentiation with respect to the radius of the crystal embryo and equating to zero allows one to determine the critical radius for a stable embryo r^*; additionally, through

the evaluation of the homogenous Gibbs free energy change expression at the critical radius r^*yields the expressions below:

$$r^* = \frac{2\gamma}{\Delta G_v}\ , \Delta G^*_{homo} = \frac{16\pi {\gamma_{ls}}^3}{3{\Delta G_v}^2}$$

Heterogeneous nucleation occurs on surfaces and interfaces other than similar sites like in the homogeneous nucleation case. Similarly, clustering on a surface is also dictated by changes in free energy and can be expressed through competitive surface terms. When the surface is a solid, the Young-Laplace formalism can be applied; here, interfacial surface energy can be balanced and the change in Gibbs free energy can be expressed below:

$$\gamma_{li} = \gamma_{si} + \gamma_{ls} cos\theta$$

$$\Delta G_{heter} = -V\Delta G_v + \gamma_{sl} 2\pi r^2 (1 - cos\theta) + \gamma_{si} \pi r^2 (sin^2\theta) - \gamma_{li} \pi r^2 (sin^2\theta)$$

$$V = \pi r^3 (2 + cos\theta) \frac{(1 - cos\theta)^2}{3}$$

Here, V is the volume, γ_{sl} is the surface energy of the solid-liquid interface, γ_{si} is the surface energy of the solid-surface interface, γ_{li} is the surface energy of the liquid-surface interface and θ is the contact angle. Similarly, navigating through the evaluation of the heterogeneous Gibbs free energy change expression at the critical radius r^*yields:

$$\Delta G^*_{heter} = (\frac{16\pi {\gamma_{ls}}^3}{3{\Delta G_v}^2}) \frac{(2 + cos\theta)(1 - cos\theta)^2}{4} = \Delta G^*_{homo}(f(\theta))$$

Naturally, heterogeneous nucleation occurs more frequently due to the additional angle dependent term $f(\theta)$. Generally, the difference between the Gibbs free energy of the liquid and the corresponding solid is a function of under-cooling; the analytical expression is written below:

$$\Delta G_v = \frac{\Delta H(T_m - T)}{T_m}$$

Here, ΔH is the latent heat of melting/fusion, T_m is the melting temperature in Kelvin and T is the temperature. [23] Specifically, when the temperature is lowered below the melting temperature, nucleation occurs more readily. Practically applying these concepts, the Bridgman-Stockbarger technique gives direct control of the spatially dependent thermal gradient, environment conditions and chemical composition. The Bridgman-Stockbarger technique is well established in industry; the Bridgman-Stockbarger technique utilizes the concept of liquid to solid transitions to produce single crystals or polycrystalline material. This method permits convective transport of source material constituents in a closed system. This process allows constituents within the melt to achieve energetically favorable positions forming crystals; essentially you are growing a crystal from a melt. In this process, nucleation can initially occur within the melt; once the crystal has nucleated from the melt, as the heat is extracted, the growth process begins and involves the transportation of solute ions/molecules from the melt to some spatial point on the surface of the produced crystal. The advantages to this technique includes the elimination of possible external contamination to the source material during growth, capitalization of buoyancy forces on relatively lighter secondary phases and large single crystal production. The Bridgman-Stockbarger apparatus is displayed in figure 3.

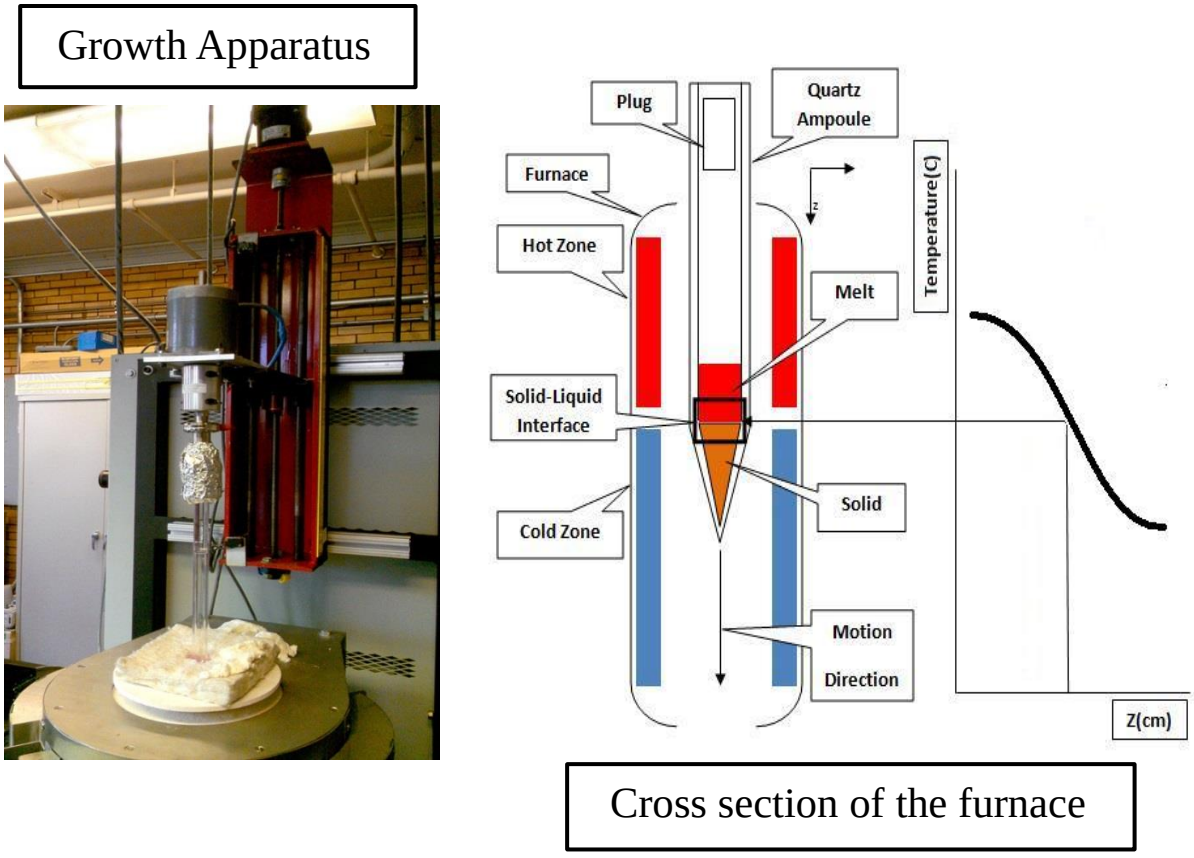

Figure 3 Illustration of the Vertical Bridgman crystal growth apparatus.

This dissertation presents theoretical and experimental studies of semi-insulating $LiIn_{1-x}Ga_xSe_2$ single crystals for neutron detection. The elements of focus are the optical properties, scintillation characteristics, and crystal growth of $LiIn_{1-x}Ga_xSe_2$ single crystals. Following this introduction, Chapter II presents experimental elements of the base compound $LiInSe_2$. Chapter III discusses the implementation of DFT calculations for $LiIn_{1-x}Ga_xSe_2$ single crystals and the consideration of isovalent gallium incorporation. Chapter IV provides experimental endeavors on $LiIn_{1-x}Ga_xSe_2$ crystal growth and a summary of the results. Therefore, the main objective of this work is to generate inorganic $LiIn_{1-x}Ga_xSe_2$ single crystals, understand their physical properties, and contribute to the efforts of producing low cost, efficient scintillator systems that can be used to detect thermal neutrons.

CHAPTER II

SCINTILLATION PROPERTIES OF SEMICONDUCTING $^{6}LiInSe_2$ CRYSTALS TO IONIZING RADIATION

Chapter II presents ionizing radiation response assessments of $^{6}LiInSe_2$ and a proof of principle demonstration for neutron detection. The content in this chapter is published as Wiggins et al. 2015 in Nuclear Instruments and Methods in Physics Research Section A: Accelerators, Spectrometers, Detectors and Associated Equipment.

Introduction

Thermal neutron detectors are important for the search for water and life in asteroids and planetary terrain, illicit nuclear material detection, neutron radiography, as well as to monitor nuclear power plant fuel processes. [2,24,25,26] A worldwide shortage of ^{3}He, currently the primary neutron detection medium, has led to great interest in solid state materials as alternative neutron detectors. [24] These alternative materials respond to incident radiation either through scintillation, where incident radiation produces visible light, or as a semiconductor, in which incident radiation produces an electric current. [26] The difficulty with most bulk materials is the competing interactions with incident gamma photons and static background induced by neutrons interacting with the surrounding environment, resulting in low neutron detection efficiency and/or poor neutron/gamma discrimination, generating the need to use multi-parameter analysis to distinguish detector response events.

Neutrons have no intrinsic charge, and therefore must be indirectly detected by converting the neutron into detectable ionizing radiation utilizing a neutron capturing isotope. The most

commonly used isotopes, for solid state alternatives, to convert neutron into detectable ionizing radiation are ^{6}Li, ^{10}B, ^{199}Hg, ^{113}Cd or ^{157}Gd. [2,26,27,28] However, Li^{6} based materials have the additive bonus of the elimination of gamma ray interactions associated with the neutron capture process of interest. ^{6}Li is within a special subset where its reaction products include an alpha particle and a triton, symbolically written as $^{6}Li(n,\alpha)^{3}H$, as opposed to a prompt gamma photon generated by the latter isotopes. As such, a smaller material volume is required to absorb the energy of the charged particles.

Lithium selenoindate is a member of the $LiB^{III}C^{VI}_{2}$ chalcogenide family. First reported to structurally exist by Hoppe, $LiInSe_2$ crystal growth has been extensively studied for applications in photonics. [29,30,31,32,33] The technical procedure for crystal growth incorporating uniform media requirements is demanding due to the corrosive nature of lithium and relatively high vapor pressure of its constituents at high temperatures, introducing purity and secondary phase production concerns. [34,35] In addition, these crystals often exhibit distinguishable variations in color and impurity content; previously published efforts have also demonstrated this common observation in $LiInSe_2$ samples. [36,37,38] Despite these difficulties, significant progress has been made concerning crystal growth and the understanding of the optical-electrical properties of this material for radiation detection. [39,40,41]

$LiInSe_2$ has the ability to respond to ionizing radiation through direct charge carrier transport; however, charge carrier trapping is demonstrated in crystals affecting the overall charge collection efficiency. [40,41] In more recent years, radiation detection viability has been investigated with the incorporation of isotopically enriched lithium-6. Due to its direct gap

characteristics, this material should undergo charge carrier recombination, producing visible light by external excitation, namely neutron detection through scintillation. [26,42] While most traditional scintillators suffer from non-proportional energy response, due to both the mobility of the charge carriers in the bulk and energy transfer to non-radiative channels , this undesirable property is avoided in semiconductors because of the ability of bulk conductivity arising from the forbidden energy gap of the material. [43,44,45,46] Therefore; in principle, narrowing the gap provides the framework to both improving the light yield in the visible spectral range and tuning the response of scintillating materials. This makes scintillating semiconductors excellent detection material templates. The absorption edge for $LiInSe_2$ at room temperature is reported to be around 2.8 eV, introducing the opportunity to explore nonproportionality in selenides and in a forbidden energy gap regime that has not yet been explored. [39,47]

Indeed, due to its unique composition as a solid state material structurally incorporating lithium-6, $^{6}LiInSe_2$ should provide the capability for neutron capture events to be observed and cleanly separated from the natural radioactivity of its neighboring constituents in the host in natural abundance, because of its large Q-value of 4.78 MeV, for the thermal neutron capture event. The next most probable thermal neutron capture process in $^{6}LiInSe_2$ is indium-115 which most frequently produces low energy prompt gammas. The transition percentages and gamma emissions of lithium-6 and indium-115 are well tabulated in the national nuclear data center website. [48] Neutron capture within the $^{6}LiInSe_2$ crystal by ^{115}In, assuming natural abundance, may account for as much as 18% of the interactions. These ^{115}In captured neutrons would not contribute to the $^{6}LiInSe_2$ detection response and would therefore limit the overall neutron detection efficiency.

This material should also support detection capabilities within a small footprint. The thermal neutron mean free path in $^{6}LiInSe_2$ is 0.09 cm. Due to the high density of the converter isotope (^{6}Li), the crystal can achieve an excellent thermal neutron capture efficiency of 99% at a crystal thickness of approximately 0.5 cm. The research presented herein demonstrates that neutron capture in $^{6}LiInSe_2$ produces a rapid scintillation response with modest light yield.

Experimental

$^{6}LiInSe_2$ crystals were grown under synthesis conditions incorporating the two step recipe explained in Tupitsyn *et al.* utilizing 95% isotopically enriched lithium-6. [41] The dimensions of the fabricated samples were measured to be 0.45x0.41x0.10 cm^3 for the yellow crystal and the red crystal was measured to be 0.60x0.60x0.06 cm^3. Representative crystals are shown in figure 4.

Figure 4 Image of representative $^{6}LiInSe_2$ crystals.

To explore the scintillation characteristics of $^{6}LiInSe_2$, the detection system was constructed by optically coupling the $^{6}LiInSe_2$ crystal to the window of a Hamamatsu 6231-100 PMT, securing a reflective surrounding and covered by an opaque enclosure to ensure the collection of the scintillated light. The luminous flux, induced by incident radiation, is converted into an electrical

signal and conditioned using a pre-amplifier, processed using an Ortec 671 shaping amplifier, supplied to a Canberra Multi-Channel Analyzer (MCA) and graphically displayed utilizing Canberra Genie software. From the irradiation of alpha particles, the timing characteristics of the scintillation event were also measured; this task was achieved by feeding the output of the PMT to a digital oscilloscope. Characteristic pulse decay times were determined by fitting the output of the pre-amplifier to a weighted linear sum of exponentially decaying terms.

To analyze the material response to ionizing radiation from different colored crystals through scintillation, X-ray Excited Optical Luminescence (XEOL) was conducted to observe allowed charge carrier transitions with a relatively high density of states. One of the advantages, exploited in this technique, is that the source photon will experience a greater mean free path as opposed to direct band edge excitation. This allows one to observe more of the bulk response to external excitation. The samples were irradiated with a Cu Kα source and the induced photoluminescence was collected through an optical fiber and process utilizing an Ocean Optics usb2000 spectrometer. In addition, these measurements were taken at room temperature (25.4^{o}C) for complementary correlation of the absorbance spectra. The room temperature absorbance spectrum was taken with a UV-Vis-NIR spectrometer (Varian Cary 500 Scan).

Results

In order to evaluate neutron induced scintillation response, the crystal was exposed to a moderated 2 Ci PuBe source using a similar pulse height spectra acquisition system. The thermal neutron flux was provided by the source enclosed in a high density polyethylene block to reduce the kinetic energy of the neutrons emitted by the source. The source was placed at the center of

the 30.5 x 45.7 x 25.4 cm^3 block. Taking the source characteristics and moderator dimensions into account, only a fraction of the neutrons incident on the crystal are thermal neutrons. [49] It should be noted that the moderated source emits a mixed field of both thermal neutrons and gamma rays.

For the neutron experiment, the detection system was constructed by optically coupling the $^6LiInSe_2$ crystal to the window of a Hamamatsu 6533 PMT securing a reflective surrounding and covered by an opaque enclosure. The scintillation response is converted into an electrical signal where an Ortec 623 spectroscopy amplifier and gated integrator collected the electrical signal for processing with an Ortec 927 Multi-Channel Analyzer (MCA) and supplied the output to a PC running Maestro software.

For the first element of investigation, the sample was exposed to a source of alpha particles and to a mixture of alpha and gamma particles. The result is displayed in Figure 5.

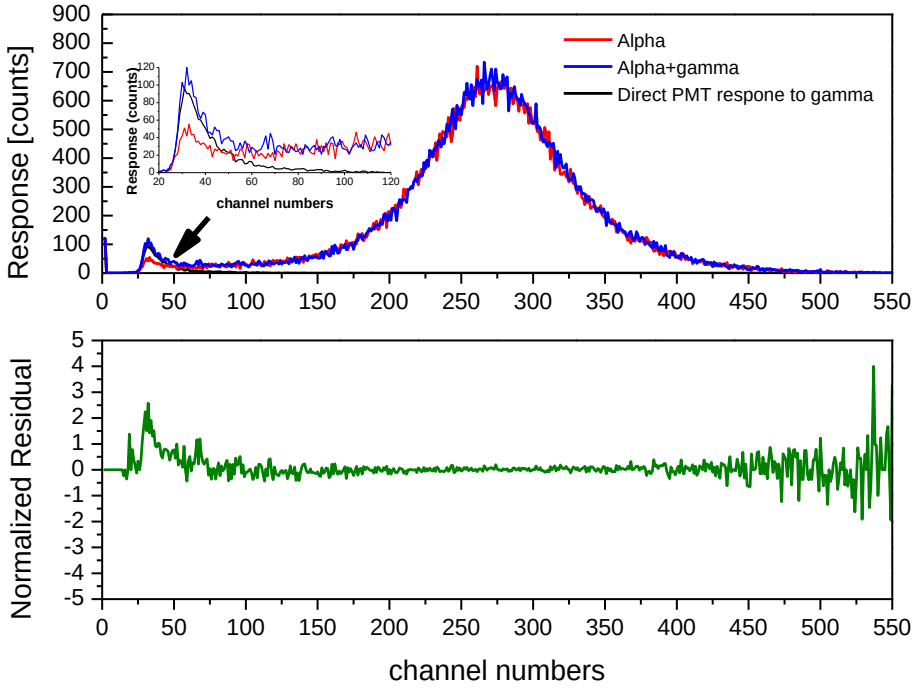

Figure 5 Pulse height spectra of $^{6}LiInSe_2$ excited with alpha particles from a ^{241}Am source and gammas from a ^{137}Cs source using a Hamamatsu 6231-100 PMT biased at 900 V and a 0 .5 μs shaping time. The alpha particle spectrum is displayed with the red line. The mixed alpha and gamma spectrum is displayed with the blue line. The normalized residual is displayed with the green line. The ^{137}Cs gamma source contribution to the PMT is displayed with the black line.

The scintillation of light produced by the irradiation of alpha particles with the 0.9 μCi ^{241}Am source showed a prominent peak with a full width at half max of 37% for the alpha peak. The alpha particle spectrum was obtained with the source directly irradiating the sample from the top crystal face, such that there was no direct alpha irradiation on the PMT area. The additional direct contribution of the 10 μCi ^{137}Cs source produced a low energy tailing contribution. The normalized residual of the two spectra is displayed with the green line to visually highlight the gamma interaction contribution. The normalized residual was obtained by dividing the residual

by a second order, Savitzky-Golay 40 point smoothed version of the alpha particle spectrum. The detection response to gamma particles is miniscule in comparison to the response to the alpha particles and is confined to low-energy channels. Based on pulse height spectral analysis alone, the ratio of the gamma induced count rate over the incident flux over the top face was calculated to be on the order of 10^{-4}. This is due to the alpha particle having a shorter range compared to gamma particles. In this gamma energy regime, the dominant gamma ray interaction is Compton scattering. This can be attributed to the small thickness of the sample (0.1 cm) and relatively low Z value of $^{6}LiInSe_2$ constituents. It is expected that pulse discrimination techniques could be employed to further differentiate gamma interactions from alpha (and neutron) response. It should be noted that the red crystal of $^{6}LiInSe_2$ was also tested and no observable scintillation response was detected. This is similar to the semiconductor radiation detection response reported for yellow and red $^{6}LiInSe_2$ crystals previously. [40]

The characteristic pulse decay profiles generated from alpha particle irradiation contained two decay constants, which were extracted to be 31±1 ns and 143±9 ns. The pulse decay profiles are displayed in figure 6. The percentage of light yield for the fast and slow component was measured to be 49% and 51% respectfully. The fast response permits a primary decay component of 143±9 ns and the opportunity for time tagging of neutron events as rapidly as approximately 30 ns, compared to approximately 400 ns for $Cs_2{}^{6}LiYCl_6$. [50] The relative light yield was measured to be 4400 photons/MeV. This value was obtained by constructing the ratio of the area under the pulse decay profile for $^{6}LiInSe_2$ compared to $Bi_4Ge_3O_{12}$. This value assumes the light yield of $Bi_4Ge_3O_{12}$ to be 9000 photons/MeV. [51] The differences in the quantum efficiency of the PMT have been taken into account concerning the incident emitted

light produced by $Bi_4Ge_3O_{12}$(480 nm) and $^6LiInSe_2$ (512 nm). Under linear assumptions, ignoring light quenching dynamics, this equates to a neutron induced light yield event of ~3900 photons/MeV for the absorption of the full Q-value for the $^6Li(n,\alpha)^3H$ reaction. While self-absorption within the bulk can be a significant factor in this result, the magnitude of the light yield estimated for the neutron event is adequate and ensures efficient detection of neutron events.

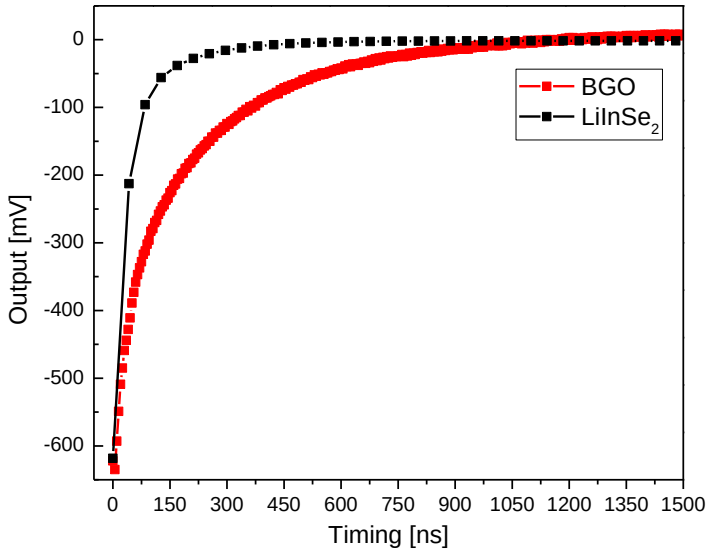

Figure 6 Pulse decay timing using a ^{241}Am alpha particle source with a Hamamatsu 6231-100 PMT 900V: The result determined two decay constants 31±1ns and 143±9ns.

Utilizing XEOL as an investigative probe, peak emission centered around 512 nm was observed in all acquired spectra for the yellow sample. Similarly, the red crystal exhibited relatively broad emission at lower energies with a peak emission centered around 662 nm. The comparison of the red crystal XEOL response to the yellow crystal XEOL response in displayed in figure 7. These transitions were also observed in the work done by Cui *et al.* and have been assigned to

donor-acceptor pair (DAP) transitions. [40] It is clear that both self-absorption and the lower energy scintillation photon response significantly affects the red crystals scintillation performance considering the quantum efficiency of the Hamamatsu PMT. Previous work related to the radiation detection properties of $^{6}LiInSe_2$ through direct charge collection also discussed crystals of distinct colors; they indicated that only the yellow crystals respond to ionizing radiation through direct charge transport acceptably well, due to a relatively higher density of deep charge carrier trapping sites in the red colored crystals. The production of these trapping sites could be a joint contribution between generated impurity complexes and constituents loss during both synthesis and growth. [40,52]

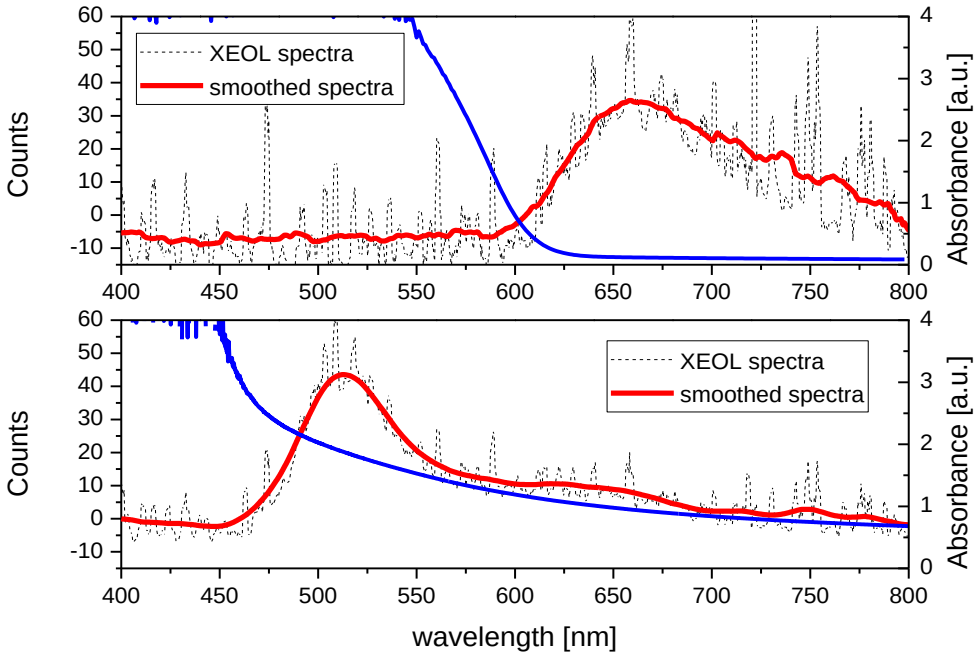

Figure 7 The top plot is the XEOL spectrum of the red $^{6}LiInSe_2$ crystal. The bottom plot is the XEOL spectrum of the yellow $^{6}LiInSe2$ crystal. The absorbance spectrum of both crystal samples are displayed with the blue solid line.

The response to neutrons is graphically displayed by the black spectrum trace in figure 8. A second spectrum was obtained by placing a 0.01 inch Cd sheet between the moderating media and the crystal to reduce the thermal neutron flux incident on the crystal. It is clear that the peak at channels 30-50 must be associated with the crystal's scintillation response to the incident neutrons because the other features in the spectrum remain unaltered by the introduction of the neutron attenuating Cd sheet. To further test this, a third spectrum was obtained with a two inch thick Pb brick positioned on top of the cadmium sheet. The Pb attenuates the gamma particles but not the neutrons, thus isolating the contribution of gamma interactions to the spectrum. The significant reduction in the low energy tail at channels 5-10 can be attributed to the interaction of gamma rays. At the same time, the static nature of the neutron peak at channels 30-50 relative to the red trace confirms that the neutron and gamma events can be separated.

The clear observation of a peak in figure 8 is a significant improvement over published results for $LiInSe_2$ crystals which determine neutron detection via charge collection directly. [41] In the published work, a clear response is observed from a neutron flux; however, poor charge collection efficiency within the crystals due to a large density of trapping sites results in a tailing continuum in the spectrum. In this case, neutron/gamma discrimination through threshold pulse height discrimination techniques cannot be applied. Here, pulse discrimination techniques are now possible with finite resolution.

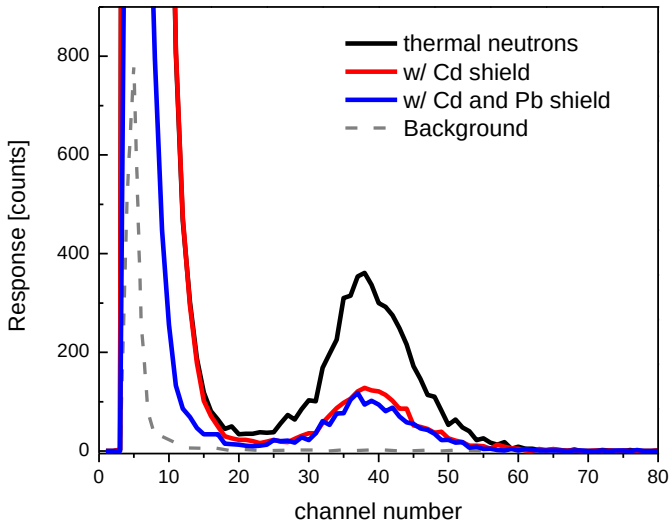

Figure 8 Pulse height spectra of the fabricated $^{6}LiInSe_2$ crystal excited from neutrons and gammas from a moderated PuBe source using a Hamamatsu 6533 PMT biased at 1600V and 0.25 μs shaping time is displayed with the black line. The pulse height spectra utilizing a 0.01 inch cadmium (Cd) shield to reduce the incident neutron flux is displayed with the red line. The pulse height spectra also utilizing a 2 inch thick lead (Pb) brick to also reduce the incident gamma flux is displayed with the blue line. The room background is display in the dashed gray line.

Conclusion

In conclusion, it has been shown that the semiconductor $^{6}LiInSe_2$ detects neutrons via scintillation. Under the $^{6}LiB^{III}C^{VI}_2$ternary compound subset, $^{6}LiInSe_2$ is the first example of a scintillating semiconductor material that detects neutrons; paving the way for a new family of chalcogenide scintillators. Utilizing XEOL, the bulk emission characteristics have been experimentally investigated with respect to $^{6}LiInSe_2$. The scintillation characteristics of

differently colored $^{6}LiInSe_2$ samples vary, where the red colored crystals incorporate negative feedback toward scintillation mechanics. For neutron detection, this material possesses the advantages of fast response, room temperature operation and compact size fabrication due to both the lithium-6 isotope being directly incorporated in its structure and its reaction products having short ranges. While current luminosity is respectable at room temperature, it can be expected to increase at cryogenic temperatures with the reduction of phonon related contributions. As development of this material continues, there must be parallel efforts to develop larger crystals with improved light yield and improve the knowledge of neutron/gamma discrimination; this is the aim for future investigations on scintillating $LiB^{III}C^{VI}_2$ crystals. The current light yield could be improved in the future and the most likely route will be to reduce the content of second phase precipitates that might contribute to optical losses. In addition, bandgap tunability using solid solutions by gallium addition, may offer an additional route for optimizing the electrical carrier generation, recombination and other relevant optical parameters.

CHAPTER III

DENSITY FUNCTIONAL THEORY INVESTIGATION OF THE $LiIn_{1-x}Ga_xSe_2$ SOLID-SOLUTION

Chapter III presents the assessment of isovalent gallium incorporation in $LiInSe_2$ to generate the $LiIn_{1-x}Ga_xSe_2$ system; the system is investigated utilizing first principle calculations within the density functional theory (DFT) framework. Utilizing the foundations of DFT, we aim to predict the compositional trend of $LiIn_{1-x}Ga_xSe_2$ single crystals; here, the $LiIn_{1-x}Ga_xSe_2$ system is represented under the subset of I-III-VI_2 compounds. The content in this chapter is published as Wiggins et al. 2016 in Physica Status Solidi B.

Introduction

The group I-III-VI_2 compounds have received a great deal of study over the past decade. Within this set, ternary lithium-containing chalcogenides with the general formula $LiB^{III}Se_2$ (B=Ga, In) are widely popular because of their promising applications in nonlinear optical devices, terahertz (THz) emission, and light-emitting diodes. [30,31,32,53,54,55] Due to lithium being directly incorporated into the structure, these lithium-containing chalcogenide materials possess great technological importance because of their significantly different thermal and optical-electrical properties compared to their heavier monovalent cation (Ag, Cu) analog, allowing them to possess relatively higher energetic phonon modes and larger forbidden gaps. [56] In recent years, focus on these ternary crystals for radiation detection applications have been additionally investigated due to their neutron detection capabilities. [40,41,57] While $LiInSe_2$ and $LiGaSe_2$ have been previously studied, historically these lithium-containing chalcogenides have various defect complexes, which can affect the optical-electrical properties. These complexes have been

seen as consequences of stoichiometric deviation. One of the many benefits of first-principle models is the assessment of various physical properties using ideal structures, providing complementary assistance to experimental understanding of compositional trends. The focal point of this investigation is the $LiIn_{1-x}Ga_xSe_2$ solid solution. Here, we look specifically at the influence of chemical disorder induced by isovalent gallium substitution.

A few experimental studies of $LiIn_{1-x}Ga_xSe_2$ crystal growth have been reported, Vedenyapin et al., then separately Wiggins et al., reported gallium substitution of the $LiInSe_2$ composition in an effort to tune optical properties experimentally. [58,59] While a complete investigation of the Li-In-Ga-Se phase space would be a tedious endeavor given the crystal growth protocols. In order to explore the entire compositional landscape of $LiIn_{1-x}Ga_xSe_2$, a Density Functional Theory (DFT) investigation has been undertaken to investigate the chemical disorder due to Ga substitution. Traditionally, chemical disorder has been utilized as a control element for band gap engineering; additionally, it has introduced complementary theoretical efforts as well. [42,60] Chemical disorder can also provide a direct pathway to improvements with scintillation characteristics, specifically the light yield and decay time; these enhancement factors have been observed in various mixed crystal systems. [61] Along with these observations, concerning the orthorhombic phase, $LiInSe_2$ and $LiGaSe_2$ have also been experimentally shown to scintillate under incident ionizing radiation, making the solid-solution an excellent template of study for chemical disorder contribution. [59,62]

In general, these I-III-VI_2 ternary compounds have been reported to have one of the four crystallographic space groups; the chalcopyrite $CuFeS_2$-type ($I\bar{4}2d$), the orthorhombic β-

$NaFeO_2$-type ($Pna2_1$), the α-$NaFeO_2$-type ($R\bar{3}m$) or cubic. The orthorhombic structure, in contrast to the cubic, chalcopyrite and α-$NaFeO_2$ structure, exhibits three nonequivalent axes corresponding to anisotropic behavior along different axes. Li et al. investigated the wurtzite type structure and determined the role of lithium within the structure to be a charge delocalization agent for stabilization; In addition, the authors describe the band gap trend of $LiB^{III}Se_2$ (B=Al,Ga,In) to be dictated by selenium 4p–atom Bs bands. [63] Additionally, the elastic, piezoelectric, vibrational and thermal properties of $LiInSe_2$ can be found elsewhere. [64,65] In this paper, the orthorhombic structured $LiIn_{1-x}Ga_xSe_2$ solid solution, belonging to the $Pna2_1$ space group, is investigated utilizing the framework of DFT and the results of these calculations are discussed.

Notably, DFT computed band gaps can be low compared to experimental results; this observable represents a general limitation utilizing DFT. To compensate for this observable, one can progressively utilize the quasi-particle GW approximation or hybrid functional approach to account for numerical discrepancies; however, these progressive endeavours generally require more computational resources as a sacrifice. None of the progressive approaches were utilized within this article. Here, numerical discrepancies were corrected utilizing experiment results.

Experimental

Growth and fabrication of the ternary and intermediate compounds were carried out by the recipe given by Wiggins et al. [59] In order to evaluate the chemical constituent distribution, scanning electron microscopy energy dispersive X-ray spectroscopy (SEM-EDX) was conducted on the intermediate compound. EDX measurements from numerous regions of the generated crystals,

over a wide range of magnification, showed little variation in the measured elemental composition. The molar indium to gallium ratio was measured through the intensity ratio of induced characteristic x-ray emission of host constituents. The indium to gallium ratio was uniform across the surface. While the lithium concentration could not be measured via EDX, it was considered to be constant across the measured region. Low-temperature optical measurements were conducted using a UV-Vis-NIR spectrometer (Varian Cary 500 Scan), a closed-cycle helium-gas cryo-cooler and vacuum-coupled cold finger with optically transparent sapphire windows; this effort was carried out to reduce the phonon contribution.

Computational details DFT calculations were carried out based on plane-wave expansions using the computer program VASP (Vienna Ab-initio Simulation Package). [66] The energy cutoff for the plane-wave basis was set to 500 eV. The exchange-correlation was treated with the assistance of both the Perdew-Burke-Ernzerhof generalized-gradient approximation (PBE-GGA) exchange-correlation potential and the local density approximation (LDA) with the Ceperley-Alder-Perdew-Zunger (CA-PZ) functional. [17,18,21] The valence electronic configurations for Li, Ga, In, and Se were Li: $2s^1$, In: $5s^2\ 5p^1$, Ga: $4s^2\ 5p^1$, and Se: $4s^2\ 4p^4$, respectively, for the projector-augmented wave (PAW) pseudo-potentials. [67] The primitive unit cell was chosen in this study to reduce the computational cost. The k-point meshes for Brillouin zone sampling were constructed using the Monkhorst-Pack scheme with a 5×4×5 k-point mesh. The total energy was minimized through varying both the cell parameters and the atomic coordinates to obtain the optimized structure by using the conjugate gradient algorithm. The self-consistent calculations were considered converged only when the total energy change was less than 10^{-8} eV, the forces on the atoms were less than 10^{-7} eV/A, and the total stress tensor was reduced to less than 0.01

GPa. The orthorhombic $LiInSe_2$ structure calculation was carried out first to evaluate the functionals and generate a reference point. The general unit cell is shown in figure 9. After completion, gallium atoms were systematically substituted for indium atoms in the lattice to achieve the desired $LiIn_{1-x}Ga_xSe_2$ composition. Within the 16 atom system, all possible isovalent configurations of indium and gallium were evaluated. The optical properties for each representative compound were also calculated through computational efforts; the calculated imaginary part of the complex dielectric function was obtained by PAW methodology. The real part of the complex dielectric function is generated from the Kramers-Kronig relation. [68]

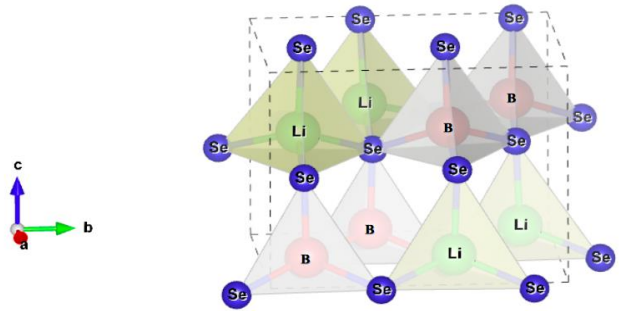

Figure 9 Illustration of the general unit cell of $LiB^{III}Se_2$ in the orthorhombic phase, where red spheres represents the B atoms (B = In, Ga), green spheres represents the Li atoms and blue spheres represent the selenium atoms. Each cation is surrounded by selenium atoms in a tetrahedral structure. The crystal is constructed by the stacking of slightly distorted, alternating tetrahedral complexes. This illustration was generated utilizing the VESTA package.[69]

Results

The orthorhombic structured $LiInSe_2$ and $LiGaSe_2$ crystals, belonging to the $Pna2_1$ space group, are related to the wurtzite structured system but differ in the base vector angle and length. Here, the orthorhombic base vector lengths are a linear combination of the wurtzite base vectors. Specifically, if the orthorhombic vector set is (a,b,c) and the wurtzite set is (a_1,b_1,c_1), these

parameters are related by $a=2a_1$, $b=a_1+2b_1$ and $c=c_1$. Additionally, while the base vector angle for the orthorhombic unit cell is 90^o, the wurtzite base vector angle is 120^o. As a figure of merit, simulations of the ternary $LiInSe_2$ and $LiGaSe_2$ compounds were included. The reduced coordinates of each type of atom are given in Table 1.

Table 1 Table of the reduced coordinates in the unit cell. The first row, for each coordinate, displays the theoretical position and the second row displays the experimentally determined position.

Calculation	Atom	x	y	z
$LiInSe_2$	Li	0.089,	0.631,	-0.005,
		0.089[70]	0.631[70]	-0.005[70]
	In	0.079,	0.126,	0,
		0.0787[70]	0.1261[70]	0[70]
	Se1	0.08,	0.128,	-0.38,
		0.0801[70]	0.1283[70]	-0.38[70]
	Se2	0.416,	0.122,	0.128,
		0.4158[70]	0.1221[70]	0.1278[70]
$LiGaSe_2$	Li	0.41,	0.878,	0.118,
		0.41[53]	0.8741[53]	0.118[53]
	Ga	0.073,	0.874,	0.623,
		0.073[53]	0.8741[53]	0.6229[53]
	Se1	-0.0936,	0.635,	0.506,
		-0.0936[53]	0.6348[53]	0.5064[53]
	Se2	0.066,	0.881,	0.991,
		0.0661[53]	0.8814[53]	0.9907[53]

The optimized lattice constants obtained from the structure calculation for all the compounds are summarized in Table 2. In consideration of the endpoints, the calculated values of the lattice

parameters in comparison with available experimental results are also shown in the table. As expected, the lattice parameters calculated through GGA somewhat overestimate the experimental values as well as the LDA predictions in much the same amount as bond distances are overestimated by GGA in molecular complexes. In addition, LDA formalism shows better agreement with the experimental results, compared to GGA formalism. For the intermediate compositions, the lattice parameters monotonically decrease with increasing gallium incorporation to reach the smaller lattice vector upon 100% substitution.

Table 2 Table of calculated structure parameters. The first row, for each lattice parameter, displays the theoretical data and the second row displays the experimentally determined lattice parameter.

composition	a(Å) GGA, LDA	b(Å) GGA, LDA	c(Å) GGA, LDA	volume(Å^3) GGA, LDA
$LiInSe_2$	7.35, 7.15	8.56, 8.29	6.94, 6.74	437.15, 399.5
	7.16227[71]	8.543[71]	6.769[71]	414.16[71]
$LiIn_{0.75}Ga_{0.25}Se_2$	7.25, 7.06	8.51, 8.24	6.86, 6.67	424.5, 388.02
$LiIn_{0.5}Ga_{0.5}Se_2$	7.17, 6.98	8.46, 8.2	6.78, 6.59	411.9, 377.18
$LiIn_{0.25}Ga_{0.75}Se_2$	7.06, 6.87	8.41, 8.15	6.73, 6.54	400.1, 366.17
$LiGaSe_2$	6.97, 6.78	8.35, 8.11	6.66, 6.48	388.28, 356.3
	6.832[53]	8.237[53]	6.535[53]	367.75[53]

It is important to note that although the lithium contribution to the density of states is weak, gallium incorporation affects the position of the valence bands. The total density of states for each compound is displayed in figure 10.

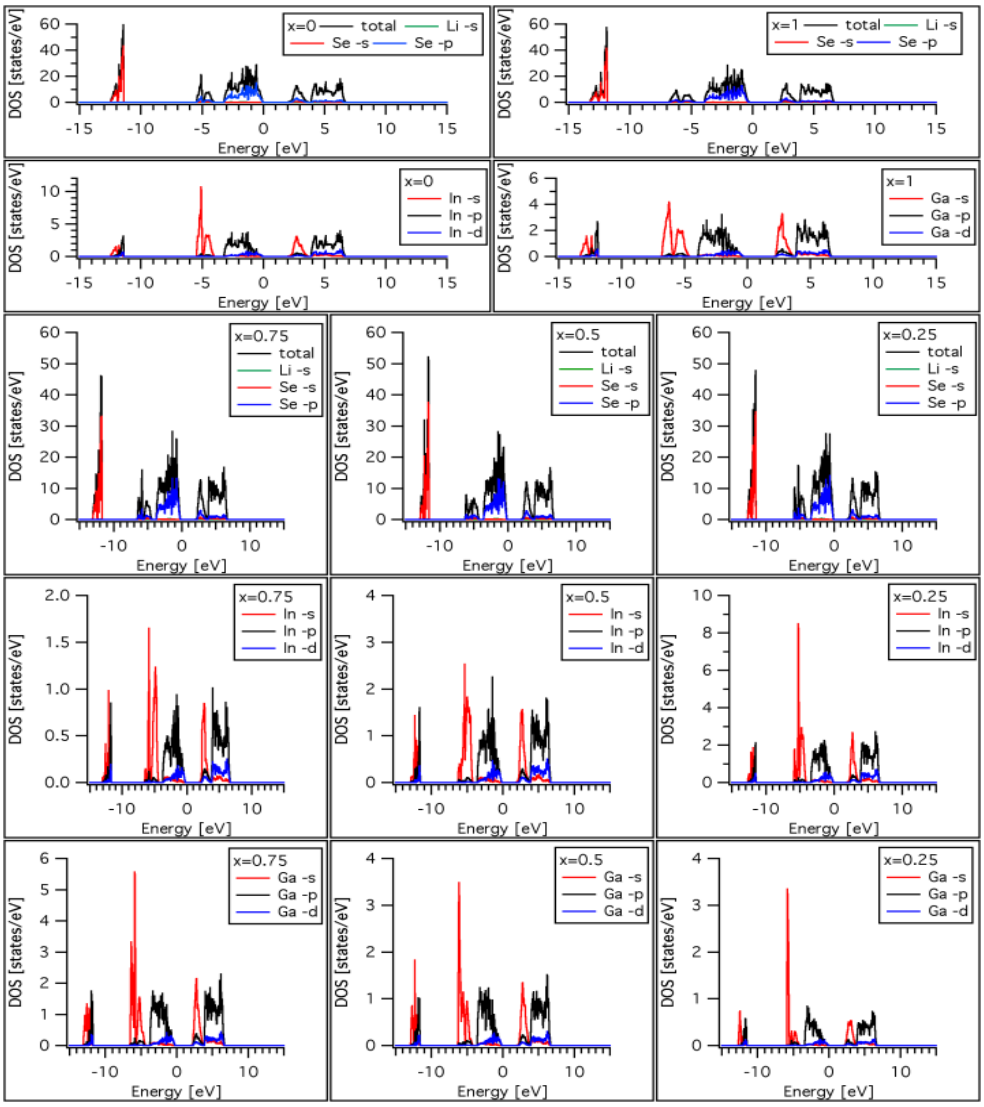

Figure 10 The total density of states and partial density of states for each representative compound is displayed, with an outlined legend in the upper right hand corner, for each corresponding composition. The total density of states and partial density of states were generated through the local density approximation. The valence band maximum is set to zero on the energy axis.

The figure displays the lowest energy configuration for each case; specifically, the variation of the ground state energy for the intermediate (x=0.5) mixed crystal spans an energy difference of

0.6 meV from the highest and lowest configuration. The (x=0.25, 0.75) intermediate mixed crystals displayed no variation. The partial density states clearly displays three occupied state distributions for all cases. The valence distribution around -11 to -14 eV represent Se-s like bands, while the two distinct distributions around 0 to -7 eV represent bonding states of the atom-B with selenium bands. Gallium incorporation reduces the Fermi energy and introduces a broadening in the distribution with respect to selenium-related electronic states near the top of the valence band due to the selenium surrounded B atom tetrahedral complexes. In comparison of the ternary parent compounds, one can visually observe the Se distributions around 0 eV to -3 eV and -4 eV to -5.5 eV broaden to 0 eV to -4 eV and -4.6 eV to -6.8 eV when moving from $LiInSe_2$(x=0) to $LiGaSe_2$(x=1). One explanation for this broadening is related to bonding characteristics, where the bond lengths for gallium are smaller than indium; this characteristic can generate a deeper potential well for the electrons, broadening these Se related states to lower energies. Comparably, moving from $LiGaSe_2$ to $LiInSe_2$, the average bond length of the B atom-Se bond was calculated to be 2.445 Å and 2.621 Å within the LDA formalism. Additionally, within the GGA formalism, the average bond length was calculated to be 2.498 Å and 2.678 Å respectively. The electronic band structure is displayed in figure 11.

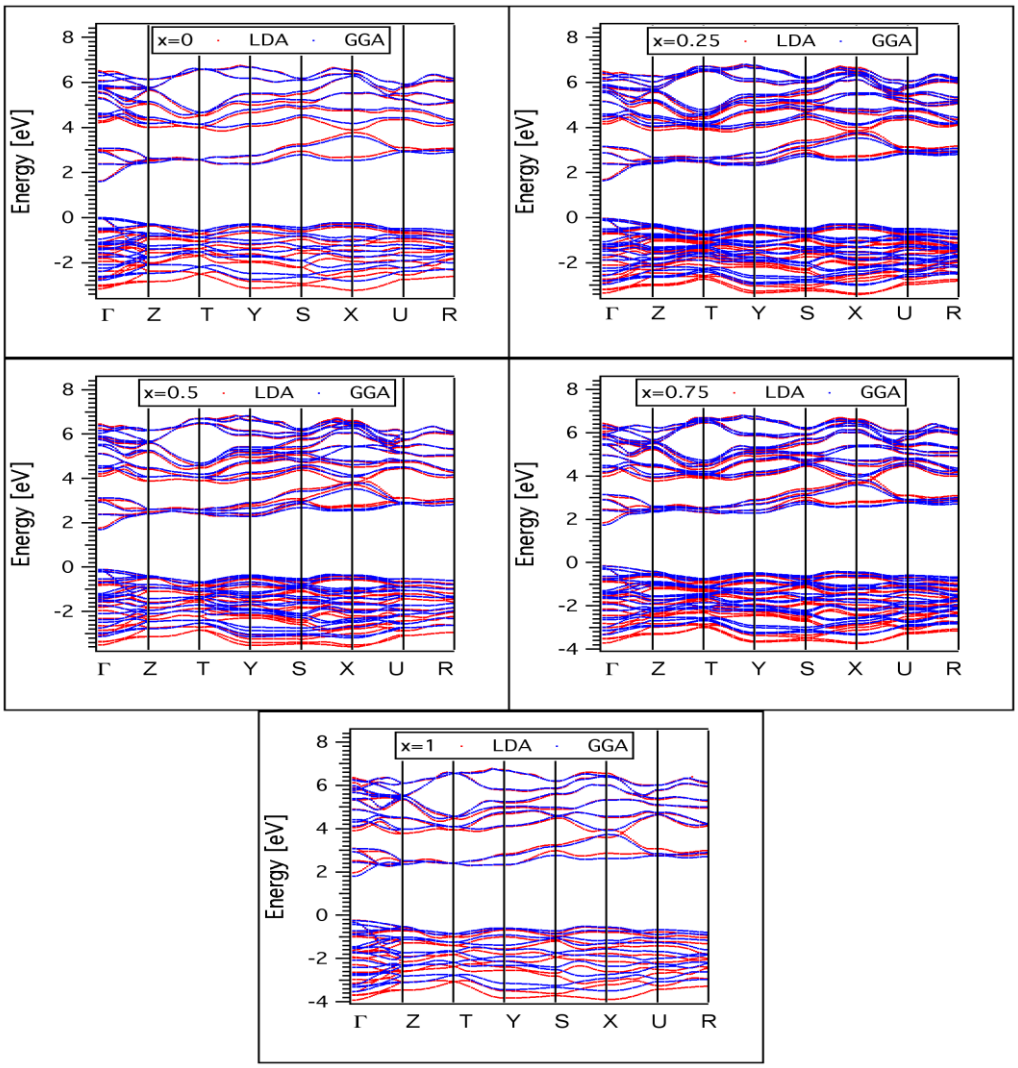

Figure 11 The band structure graphs for each representative compound are displayed in red and blue traces. The valence band maximum is set to zero on the energy axis. The red trace is the band structure calculation utilizing the local density approximation. The blue trace is the band structure calculation utilizing the generalized gradient approximation.

The energy separation from the top of the valence band to the bottom of the conduction band is defined as the band gap. Here, these extrema are located at the Γ point. As the gallium concentration increases, the energy separation at the Γ point increases. Upon inspection of the

band structure, luminescence can clearly be expected, even at low temperatures, due to the direct gap characteristics these crystals possess at the Γ point; previous experimental studies have also demonstrated photoluminescence for the $LiInSe_2$(x=0) case. [40,62] Because luminescence can be expected from these tetrahedral complexes, these bond lengths have a direct influence on charge carrier transition frequency; through changes in the local electric field by gallium incorporation, one can tune emission and shorten decay lifetimes.

While the calculated values are relatively low compared to experimental values, the compositional trend can provide bowing information related to the solid solution. Using the equation provided below, it is possible to estimate the deviation from linear behavior.

$$(1-x)\left(E_g^{(LiInSe_2)}\right) + (x)\left(E_g^{(LiGaSe_2)}\right) - \ b\,x(1-x)$$

Here, the estimated bowing values for the $LiIn_{1-x}Ga_xSe_2$ system are between 0.14 +/- 0.03 with respect to GGA formalism and 0.2 +/- 0.04 for the LDA formalism. Table 3 summarizes the calculated results of the band gap at the Γ point. For the intermediate compounds, the band gap values were estimated through a correction by calculating the difference of the ternary compound experimental values and the calculated result. From the ternary endpoints, the difference was assumed to follow a linear dependence. The correction was carried out by adding the difference to the calculated result, followed by adding the corresponding bowing value. The minimum and maximum bowing values were considered.

Table 3 Table of calculated and experimental gaps.

composition	characteristic	LDA(eV)	GGA(eV)	Experimental(eV)
$LiInSe_2$	Direct	1.63	1.6	2.99
$LiIn_{0.75}Ga_{0.25}Se_2$	Direct	1.73	1.69	3.08-3.11
$LiIn_{0.5}Ga_{0.5}Se_2$	Direct	1.87	1.8	3.21-3.24
$LiIn_{0.25}Ga_{0.75}Se_2$	Direct	2	1.91	3.37-3.39
$LiGaSe_2$	Direct	2.19	2.05	3.56

These results provide a first look at the functional dependence of the band gap through strain contribution. The magnitude of the bowing parameter is comparable to traditional materials but provides a clearer understanding on experimental results to constrain the band gap trend of the $LiIn_{1-x}Ga_xSe_2$ solid-solution system. [42,60] Compared to nitride alloys, which have bowing values on the order of 1 eV, this result suggests that the $LiIn_{1-x}Ga_xSe_2$ system has a relatively moderate dependence on strain.

The calculated real and imaginary part of the dielectric function, for each $LiIn_{1-x}Ga_xSe_2$ compound, is displayed along with the static, directionally averaged real part as a function of gallium content in figure 12. The imaginary part of the dielectric function provides information on intraband transitions and taking the square root of the real part of the dielectric function yields the index of refraction within the low-frequency regime. For the $LiIn_{1-x}Ga_xSe_2$ system, the dielectric constants can potentially be used to determine the composition.

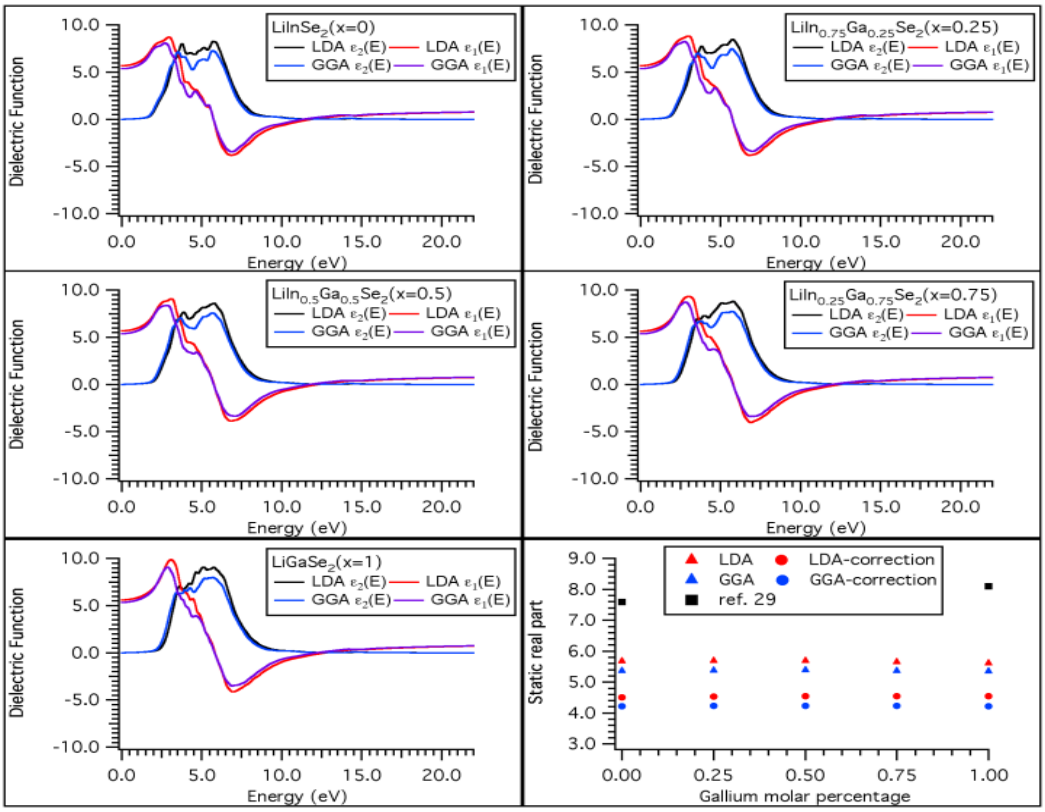

Figure 12 The real (ε_1) *and imaginary* (ε_2) *dielectric components for each representative compound are displayed in red, blue, black and purple traces. The red and black traces are the real and imaginary components respectively, utilizing the local density approximation. The blue and purple traces are the real and imaginary components respectively, utilizing the generalized gradient approximation. The bottom right hand graph displays the static real part as a function of gallium concentration for each functional respectively. The triangle markers represent the initial calculation and the circle markers represent the imaginary part onset corrected result. The black squares represent available experimental data.*

The blue shift in the calculated imaginary part of the dielectric function corresponds to the absorption edge at the Γ point followed by additional critical points where the density of states is large in the dispersion relationship. Observable differences between the GGA and LDA

outcomes are shown. They are slightly different because the calculated band gaps for both formalisms are slightly different; this observation arises from the differences in the calculated lattice parameters. Considering that the LDA and GGA results underestimate the band gap, consequently underestimating the onset of the imaginary part of the dielectric function, this can overestimate the value of the real part of the dielectric function through the Kramers-Kronig relation. To correct for this result, one can shift the onset of the imaginary part of the dielectric function to the appropriate value given in Table 3 then recalculate the real part via the Kramers-Kronig relation. The calculated real part of the dielectric function provides a comparative quantity to experimental efforts. Comparing the ternary compound results to the study carried out by Kamijoh et al. [72], the calculated values of the static real part of the dielectric function are lower than the experimental results by almost a factor of two. To the best of our knowledge, no additional static measurement is known. Notably, our calculated dielectric constant only represents the electronic contribution and does not include phonon contribution; the calculated quantity is also known as the high frequency dielectric constant. Comparing available index of refraction measurements in transparent intervals, squaring the directionally average value for comparison, our calculated high frequency dielectric constant is within good agreement. [32] The ratio of the static dielectric constant over the high frequency dielectric constant is comparable to similar material types, such as the II-VI compounds. [42]

The calculated and experimentally obtained absorption coefficient at 7K is displayed in figure 13.

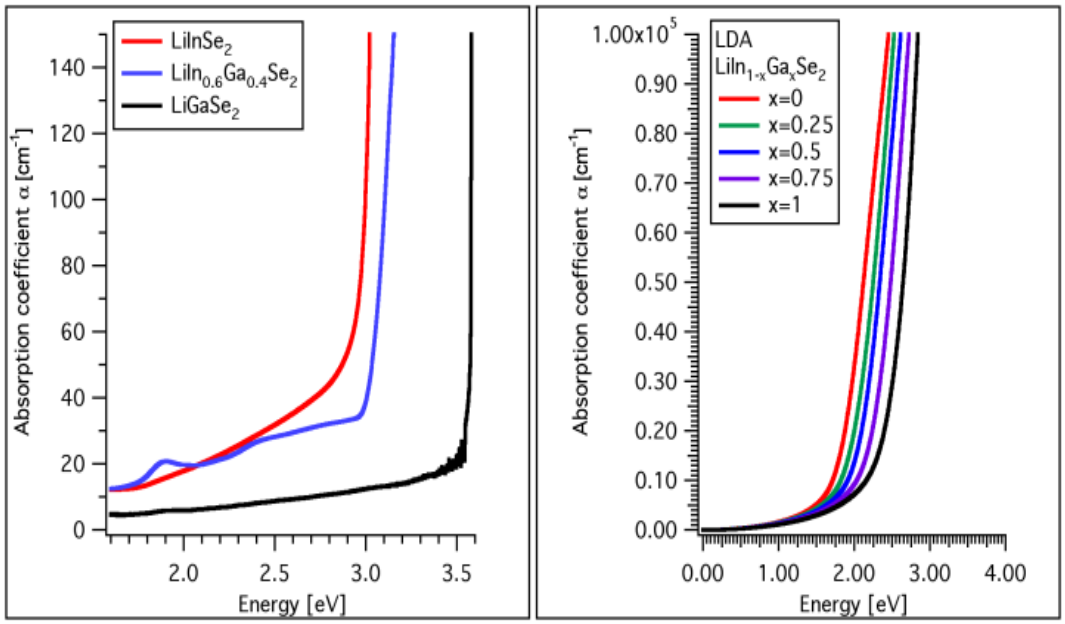

Figure 13 The absorption coefficient as a function of energy is displayed at 7K for generated crystal compositions on the left. The calculated absorption coefficient within the local density approximation is displayed on the right. The absorption edge shifts as a function of gallium concentration, indicating a change in the energy separation of the local extrema located at the Γ point.

The bandgap of 2.99 eV and 3.56 eV correspond to $LiInSe_2$ and $LiGaSe_2$, respectively. The intermediate compound $LiIn_{0.6}Ga_{0.4}Se_2$ yielded a bandgap of 3.08 eV. The theoretical band gap for the x=0.4 case lies between 3.16-3.19; comparing the experimentally determined result, the difference agrees within 2-3.5 percent. The best fitted trend line determined the temperature dependent shift from room temperature (300 K) to be 6.48×10^{-4} eV/K for the ternary compounds and 4.14×10^{-4} eV/K for the intermediate compound. The lower value for the intermediate

compound is directly influenced by the incorporated strain. It seems plausible to suggest that the local potential disorder influences the heat capacity at constant pressure to increase. With progressive development, the heat capacity may also serve as a parameter of control for strain in the $LiIn_{1-x}Ga_xSe_2$ system.

Conclusion

Theoretical calculations have been carried out for pure static crystals at zero kelvin with no phonon contribution consideration. The electronic and optical properties were calculated by first principles. Chemical disorder in the $LiIn_{1-x}Ga_xSe_2$ solid-solution system was investigated; the effects directly influenced the lattice parameters and direct gap transitions at the Γ point. The bowing parameter for this material system has been constrained to 0.1-0.3 eV. This result reinforces the capability of alter the density of states and tune the absorption characteristics through gallium contribution. Low-temperature optical absorption confirmed this trend and revealed a change in the heat capacity at constant pressure. The results also show that induced strain, through gallium contribution, can alter the heat capacity of this system as well.

CHAPTER IV

GROWTH OF $LiIn_{1-x}Ga_xSe_2$ SEMI-INSULATING CRYSTALS

This chapter provides an overview of crystal growth endeavors to generate $LiIn_{1-x}Ga_xSe_2$ single crystals and experimental characterization of generated $LiIn_{1-x}Ga_xSe_2$ compositions. The content in this chapter has been submitted to the journal of crystal growth.

Introduction

The growth of ternary lithium containing chalcogenides (Li-III-VI_2) have been studied extensively within the literature; within this ternary compound subset, $LiB^{III}Se_2$ (B = In, Ga) compounds have been pursed for various optical applications such as terahertz emission, second harmonic generation and for parametric oscillators due to their nonlinear optical response. [30,31,32,54,55] In addition, $^6LiInSe_2$ and $^6LiGaSe_2$ have also been explored for neutron detection applications. [41,47,59,62] For these detection applications, a novel two step synthesis was developed in order to better control lithium reactivity. [73] The binary alloy LiIn (or LiGa) is prepared initially, followed by slow addition of the chalcogenide via vapor transport. The authors note that the improved crystal purity results in a reduction of defects which act as trapping sites for the charge carriers created in the $^6Li(n, \alpha)$ nuclear reaction. $^6LiInSe_2$ has been reported to detect thermal neutrons as both a semiconductor and scintillator. [47,62] While it is a promising novel material, $^6LiInSe_2$ has the disadvantage of containing indium. The ^{115}In isotope also captures neutrons; however, gamma rays and betas are generated which do not contribute to the neutron detection mechanism thereby limiting the overall neutron detection efficiency. [62,74] Due to this fact, the effective neutron detection efficiency of $^6LiInSe_2$ is limited to 82 percent due to neutron capture by indium atoms within the material matrix. $^6LiGaSe_2$, on the

other hand, has no significant neutron absorption and represents an excellent improvement in comparison to the neutron capture contributions in $^{6}LiInSe_2$. In consideration of the $^{6}LiGaSe_2$ case, recent results have shown that $^{6}LiGaSe_2$ does not respond to radiation through scintillation strongly compared to $^{6}LiInSe_2$. [59] Additionally, $^{6}LiGaSe_2$ operating through direct charge carrier transport demonstrates instability under applied bias; these observations highlight significant bulk polarization and suggest higher ionic mobility compared to $LiInSe_2$.

Considering these elements, $^{6}LiIn_{1-x}Ga_xSe_2$ represents the key to understanding the compositional trend and addresses the neutron capture limitation. Substitution of indium with gallium supports the generation of the $^{6}LiIn_{1-x}Ga_xSe_2$ solid-solution; here, external control of the In/Ga ratio allows one to alter the electronic structure which dictates the optical properties and control the indium neutron activation contribution. Historically, due to the volatile and reactive constituents of lithium containing chalcogenides, crystal growth has been viewed as difficult; however, considerable progress has been demonstrated, by the vertical Bridgman technique, on the growth of lithium containing chalcogenides and their solid-solutions [30,31,58,75]

Considering potential reaction pathways, there are various routes to synthesize the $LiIn_{1-x}Ga_xSe_2$ material; these pathways include the reaction between Li_2Se, Ga_2Se_3 and In_2Se_3 in proper molar portion, the mixture of the $LiInSe_2$ and $LiGaSe_2$ compounds or the direct synthesis from elementary reagents. Considering the first approach, using binary compounds, this task is difficult due to the sensitivity of Li_2Se to ambient moisture and extremely high melting point. While the second approach is also possible, these ternary compounds suffer from incongruent

sublimation, increasing the possibility of secondary phase generation. Lastly, the black caldron approach, utilizing elemental reagents can also lead to uncontrollable secondary phase formation due to the extreme reactivity of lithium. [41,57] Vedenyapin et al. reported on a $LiIn_{1-x}Ga_xSe_2$ composition, $LiIn_{0.5}Ga_{0.5}Se_2$ in the text, demonstrating feasibility but notes a gallium concentration of 42-43 percent utilizing lattice parameter analysis. One of the benefits of the $LiIn_{1-x}Ga_xSe_2$ system is that this mixed system has a lower melting point as opposed to its ternary parent compounds. [58] The advantage of relatively lower melting temperatures, due to the quaternary eutectic, allows one to reduce the vapor pressure during synthesis and growth procedures, thus reducing the loss of constituent elements that might cause deviations from stoichiometry and reactivity with the crucible.

Initial investigations of the $LiIn_{1-x}Ga_xSe_2$ system have shown that this material system scintillates when under an incident flux of ionizing radiation. [59] This confirms that the $LiIn_{1-x}Ga_xSe_2$ solid solution can be utilized as a template to study disorder contributions to scintillation and provides a potentially progressive framework to improving the neutron detection efficiency. [61] The present work extends on the $LiIn_{1-x}Ga_xSe_2$ material system for radiation detection viability. The research presented herein demonstrates an alternative pathway for the synthesis and growth of $LiIn_{1-x}Ga_xSe_2$ compounds.

Experimental

In order to investigate the overall neutron capture efficiency in $^6LiIn_{1-x}Ga_xSe_2$ compositions, MCNP6 simulations were carried out. The MCNP6 tool kit and standard neutron cross sections

were employed, through the F2 tally, to calculate the neutron capture efficiency of $^{6}LiIn_{1-x}Ga_xSe_2$ compositions. [76] The simulations assumed a composition of 95% isotopically enriched lithium-6, with indium, gallium and selenium in natural abundance. The simulations mimicked a simple transmission apparatus in vacuum with a 1mm sample; F2 flux tallies were constructed on opposite faces of the crystal. The density of the mixed compound was assumed to follow a weighted average of the parent compounds—$^{6}LiInSe_2$ and $^{6}LiGaSe_2$—depending on their molar percentage. In addition, the functional dependence of the neutron attenuation is assumed to be similar to photon attenuation. The percent capture efficiency quantity was generated by subtracting the transmission portion from unity. The same simulation was utilized to generate the linear attenuation coefficient as a function of incident photon energy with the energy range of 0.1 to 10 MeV.

Concerning material synthesis, the initial reagents utilize in this study were lithium (4N), gallium (5N), indium (6N) and selenium (6N); all reagents were purchased from industry. The synthesis of the quaternary compound followed a two-step procedure. This first step was the synthesis of the $LiIn_{1-x}Ga_x$ alloy, with the proper corresponding molar ratio, in a pyrolotic boron nitride (PBN) crucible. In response to the volatile nature of lithium, an additional 4% of the stoichiometric weight was added to the charge. The material charge, within the PBN crucible, was then loaded into a quartz ampoule. The ampoule system was initially evacuated to a residual pressure of 10^{-5} Torr and then sealed with a 0.5 bar of argon pressure inside the ampoule. The closed ampoule system was then loaded into a muffled furnace and set to a temperature of 750 °C; the ramp rate of this synthesis procedure was 0.5 ^{o}C/min.

$LiIn_{1-x}Ga_xSe_2$ samples were synthesized by using the generated alloy material ($LiIn_{1-x}Ga_x$) and adding selenium (Se) via physical vapor transport. Specifically, the selenium vapor reacts with the generated alloy material while the alloy sits in a PBN crucible; the synthesis of the quaternary compound was also conducted in a closed ampoule system with a 0.5 bar of argon pressure inside the ampoule. The closed ampoule system was then loaded into a muffled furnace that was set to a temperature of 940°C; the ramp rate of this synthesis procedure was set to 0.5 ^oC/min to reduce the volatile nature of selenium induced by rapid heating. One element that represents a significant parameter for the quaternary compound is the degree of mixing during the synthesis procedure. To ensure good mixing, during the heating and soaking phase of both synthesis procedures, the material charge was rotated at approximately 15 rpm at a 45 degree angle. The allocated soaking time for both synthesis procedures was one hour and continued with a cooling procedure set to 3.5 ^oC/min.

Growth of the quaternary compound was executed with a two zone furnace by the vertical Bridgman technique. The furnace utilized resistive coils, in temperature controlled zones, in a practically thermally isolated enclosure. The hot zone was set at a temperature of 940 ^oC and the cold zone was set at 760 ^oC. The vertical growth translation rate was 0.7 cm/day. After translation, the crystals were slowly cooled to room temperature. The crystalline samples were fabricated by procedural polishing and etched in 5% Bromine-Methanol solution. The ternary $LiInSe_2$ and $LiGaSe_2$ compositions were prepared as reference samples across the quaternary $LiIn_{1-x}Ga_xSe_2$ stoichiometric regime; intermediate compositions with gallium concentrations of 25, 50 and 75 percent were additionally prepared in order to understand how the optical properties could be tuned. A summary of the generated compounds in this study is shown in

figure 14. One notable feature is the color change as gallium systematically replaces indium; this observation indicates a change in the absorption edge. Complementary to this observation, an additional feature is the clear color of $LiGaSe_2$ which in previous crystal growth efforts were reported to be yellow. [41]

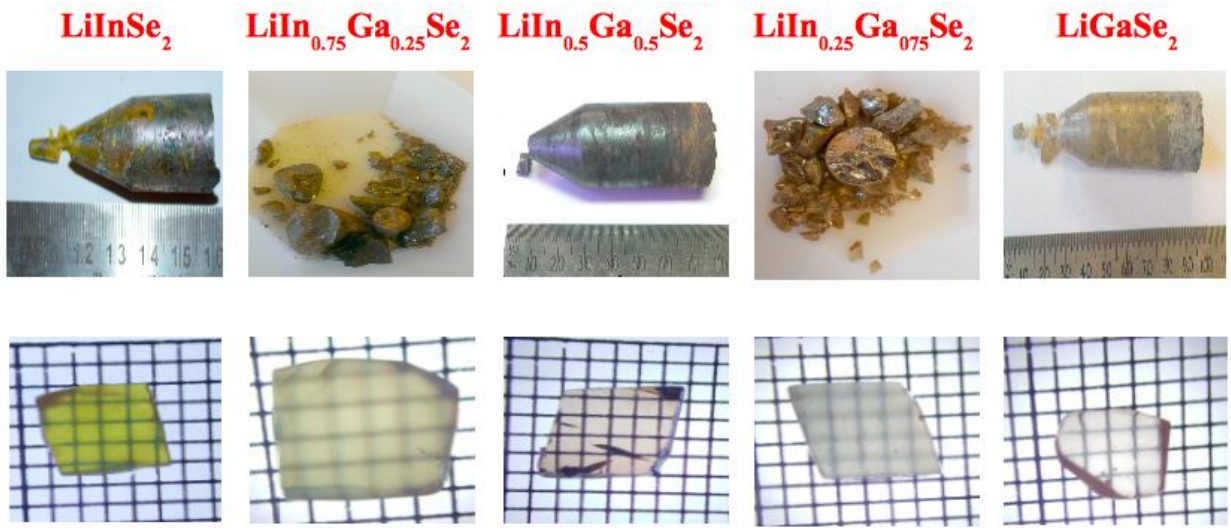

Figure 14 displays the crystal growth yield and a polished crystal for each $LiIn_{1-x}Ga_xSe_2$ composition; however, the quality and size of the crystals varied from 1 mm^3 or larger. The grid below is 1mm x 1mm. The composition in the red font represents the initial composition.

A representative sample of each stoichiometry was collected and analyzed. Powder x-ray diffraction (XRD) was used to obtain structural information on the intermediate quaternary compounds and reference ternary compounds; the diffraction data was refined through GSAS. [77,78] For the task of determining chemical content, scanning electron microscopy (SEM) and energy dispersive x-ray spectroscopy (EDX) was utilized. To determine phase transition information, differential scanning calorimetry (DSC) was used; for the DSC measurement, a

TGA-DSC 987 TA instrument was used with a heating and cooling rate of 10^{o}C/min. The optical absorption spectra were taken at room temperature utilizing a UV-Vis-NIR spectrometer (Varian Cary 500 Scan).

Results

Figure 15 displays simulations results of the neutron capture efficiency as a function of incident neutron energy for a series of representative $^{6}LiIn_{1-x}Ga_xSe_2$ samples. The systematic replacement of indium with gallium reduces the neutron capture contribution of indium; this is illustrated with localized indium resonances decreasing as the atomic concentration of indium is systematic replaced with gallium. Figure 16 displays the thermal neutron capture contribution of indium as a function of gallium molar percentage. Calculations revealed that the upper bound of the neutron detection efficiency can increase from 80% to 97% through the removal of indium capture events and utilization of the $^{6}Li(n,\alpha)$ reaction. The efficiency calculations agreed well with analytical calculations. The linear attenuation coefficient for gamma rays is shown for each $^{6}LiIn_{1-x}Ga_xSe_2$ composition in figure 17.

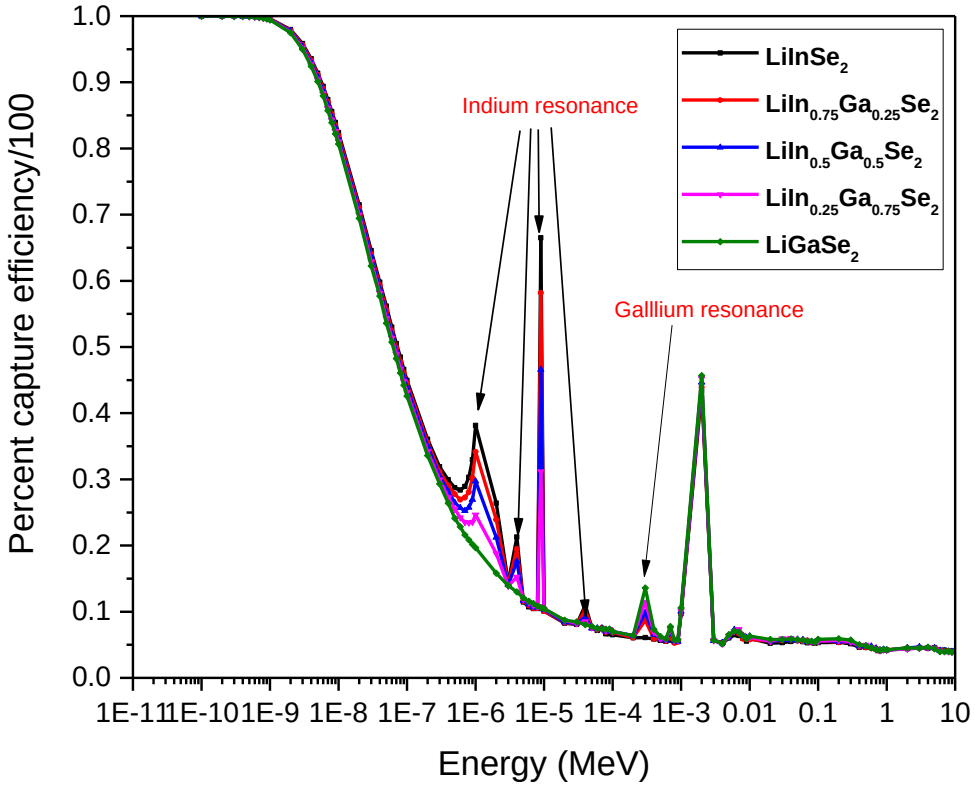

Figure 15 displays the neutron capture efficiency displayed as a function of incident neutron energy. Each trace is representative of a unique $LiIn_{1-x}Ga_xSe_2$ *sample composition with a thickness of 1mm.*

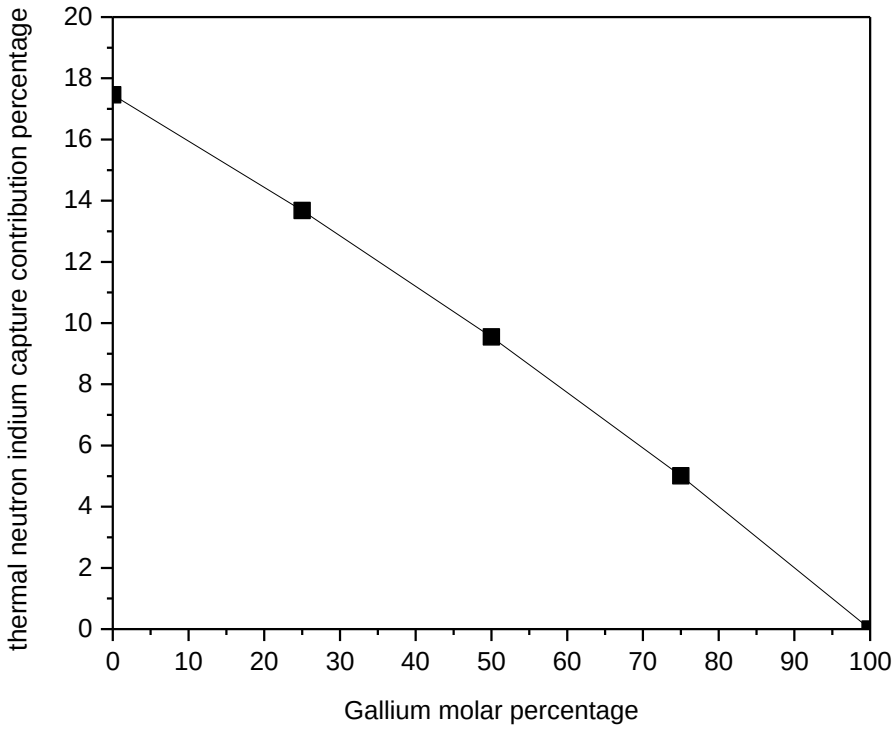

Figure 16 displays the indium contributions to thermal neutron capture as a function of the molar percentage of gallium in representative $LiIn_{1-x}Ga_xSe_2$ compounds.

Due to the reduction in charge density, the replacement of indium with gallium reduces the gamma interactions in this material system. Here, the $^6LiIn_{1-x}Ga_xSe_2$ system with ($x > 0$) is expected to be less susceptible to the absorption of incident gamma photons. $^6LiGaSe_2$ possesses the longest mean free path for photon interaction; this result is clear for the low energy gamma regime [0.1 MeV] in Figure 3. Comparably, moving from $^6LiInSe_2$ to $^6LiGaSe_2$, the expected mean free path for a 0.1 MeV photon ranges from 2.3 mm to 4.1mm.

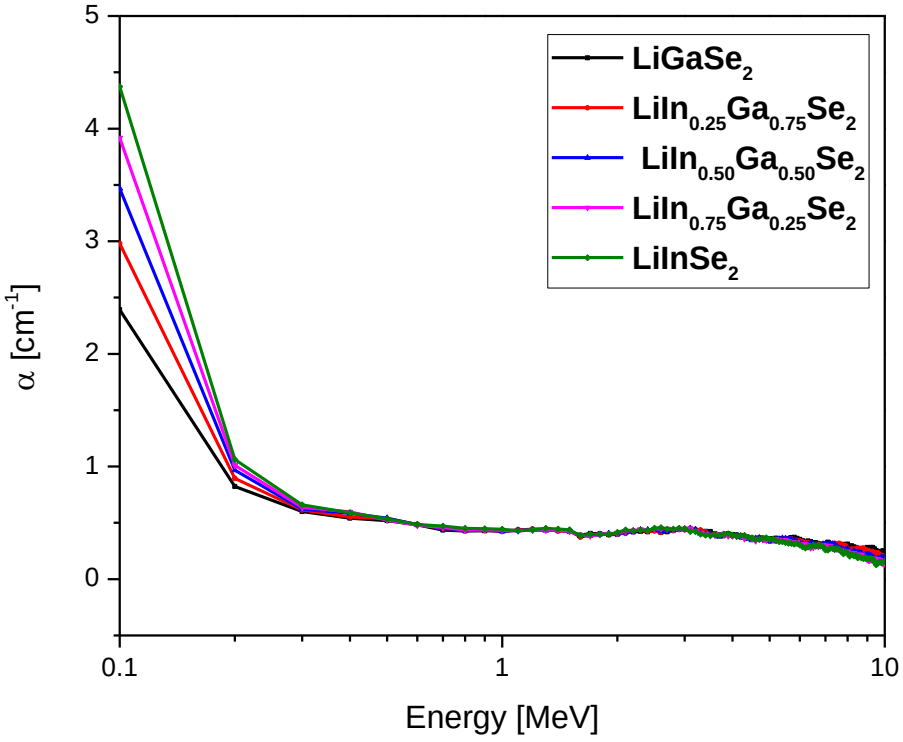

Figure 17 displays the calculated linear attenuation coefficient as a function of incident photon energy. Each trace is representative of a unique $LiIn_{1-x}Ga_xSe_2$ sample composition with a thickness of 1mm.

Powder x-ray diffraction (XRD) measurements indicated that each $LiIn_{1-x}Ga_xSe_2$ composition resulted in a single phase compound. XRD peak positions of $LiInSe_2$ matched the orthorhombic phase and agreed with previously published lattice parameters: a=7.192 Å, b=8.412 Å, c=6.793 Å. [36] Similarly, the $LiGaSe_2$ crystal also agreed with published orthorhombic lattice parameters: a = 6.833 Å, b = 8.227 Å, and c = 6.541 Å. [79] The powder XRD pattern for each of the mixed $LiIn_{1-x}Ga_xSe_2$ compositions prepared showed a single phase with the Bragg peaks shifted to smaller two theta values indicating lattice parameter contraction; the lattice parameters

shrink with increasing gallium concentration. The extracted lattice parameters are displayed in figure 18.

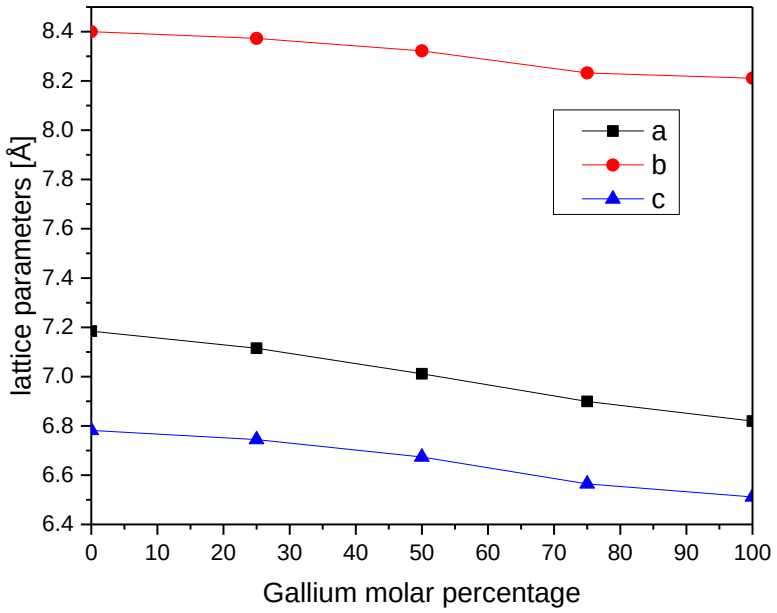

Figure 18 displays the extracted lattice parameters for $LiIn_{1-x}Ga_xSe_2$ crystal powder. The result displays a systematic lattice parameter decrease as the gallium concentration increases in value.

In order to evaluate the chemical constituent distribution, SEM and EDX was conducted on the $LiIn_{1-x}Ga_xSe_2$ samples. Figure 19 shows an SEM image of representative $LiIn_{1-x}Ga_xSe_2$ samples along with the complementary EDX maps of the investigated region. Host constituents such as indium, gallium and selenium are observed over the bulk of the image. While the lithium concentration could not be measured via EDX, it was considered to be constant across the measured region. EDX maps from numerous regions of the representative crystal, over a wide range of magnification, showed little variation in the measured elemental composition for all

gallium concentrations; however, due to the differences in initial composition compared to the measured composition, finite segregation is observed within the system. Gallium segregation is possible considering the ionic radius mismatch of the trivalent In^{3+} ion and the trivalent Ga^{3+} ion; here, the ionic radius ratio of the gallium ion to the indium ion is around 19 percent. This observation strongly suggests vertical segregation of the gallium constituent. The measured composition was obtained through a spatial location average. Concerning the compositional variation of the generated quaternary samples, the $LiIn_{0.6}Ga_{0.4}Se_2$ composition displayed the least amount. Notably, the standard deviation of the $LiIn_{0.6}Ga_{0.4}Se_2$ composition was 3 to 4 times lower compared to the other quaternary samples.

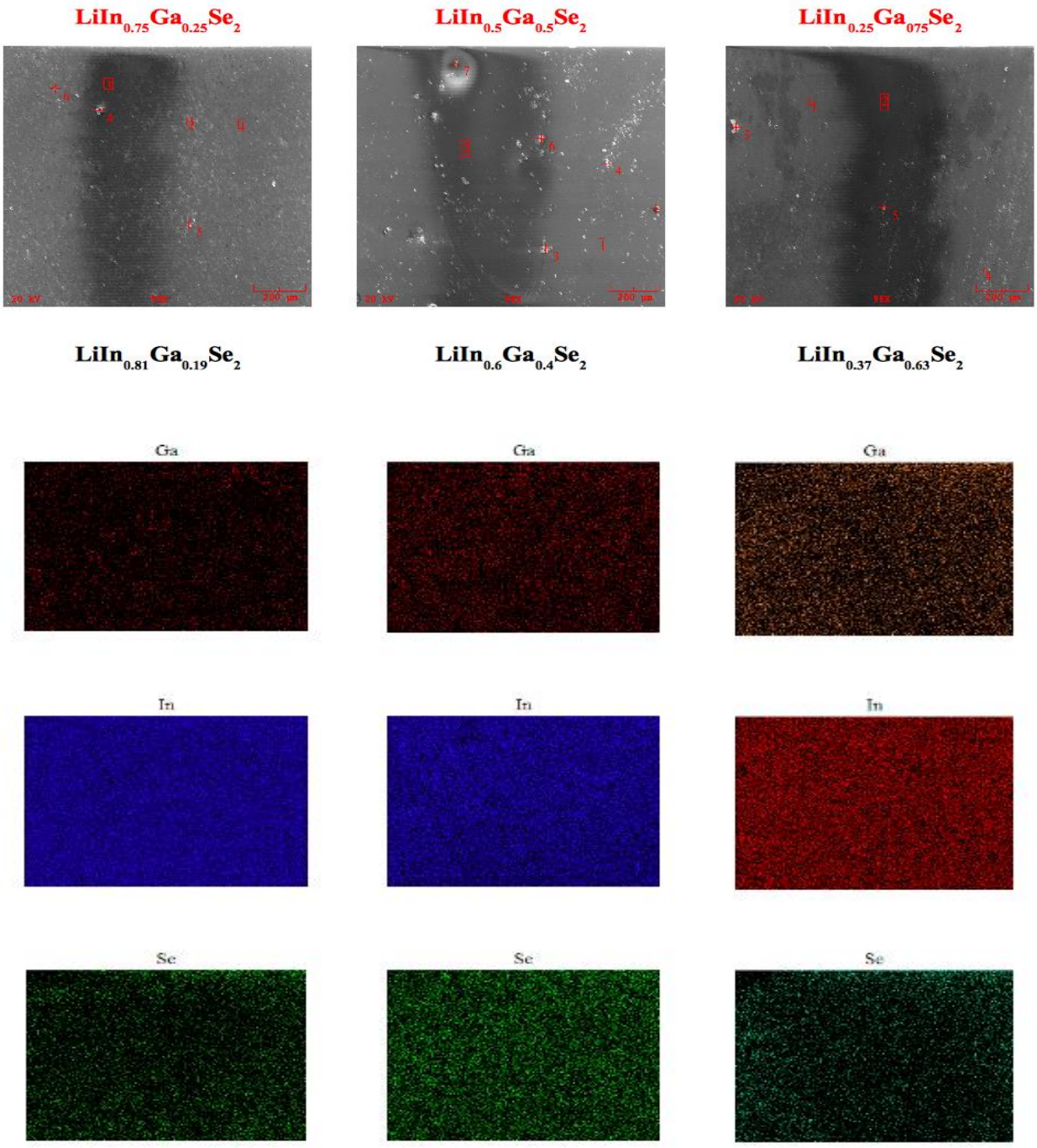

Figure 19 displays the elementary host constituent distribution for each mixed $LiIn_{1-x}Ga_xSe_2$ composition, moving from the left to right column. The composition in the red font represents the initial composition and the composition in the black font represents the measured composition through EDX. The first row displays the SEM image; row 2 through 4 displays elemental maps.

The transition points of $LiIn_{1-x}Ga_xSe_2$ compositions were measured using differential scanning calorimetry. In all cases, a melting transition for the quaternary chalcogenide was observed. The peak melting temperatures are displayed in figure 20 and demonstrate a slight melting peak depression trend from $LiInSe_2$ (x=0) toward the eutectic case (x=0.5). Vedenyapin et al. reported a melting point of 830 ^oC for the $LiIn_{57-58}Ga_{42-43}Se_2$ crystal, which is relatively lower than the value reported here in. [58] The higher melting point, which is consistent with other Li-containing chalcogenide crystals, suggests the present work resulted in a relatively more pure product.

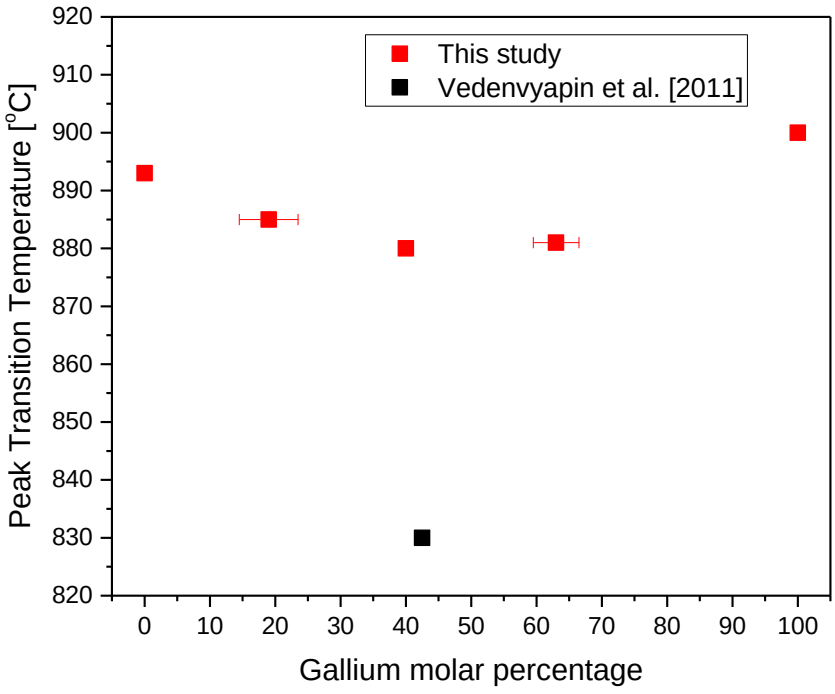

Figure 20 displays the peak melting transition temperature of $LiIn_{1-x}Ga_xSe_2$ crystals.

The room temperature absorption coefficient and corresponding band gap for each representative compound is given in figure 21. The band gap of 2.85 and 3.38 eV correspond to $LiInSe_2$ and $LiGaSe_2$, respectively, and are in reasonable agreement with the published band gaps for stoichiometric crystals. The absorption edge trend shows a blue shift with increasing gallium concentration. The large scattering features observed for the x=0.19 case is most likely due to induced scattering through compositional variation. Here, the x=0.19 case demonstrated the most observable segregation and possess the largest variation with respect to the average compositional value.

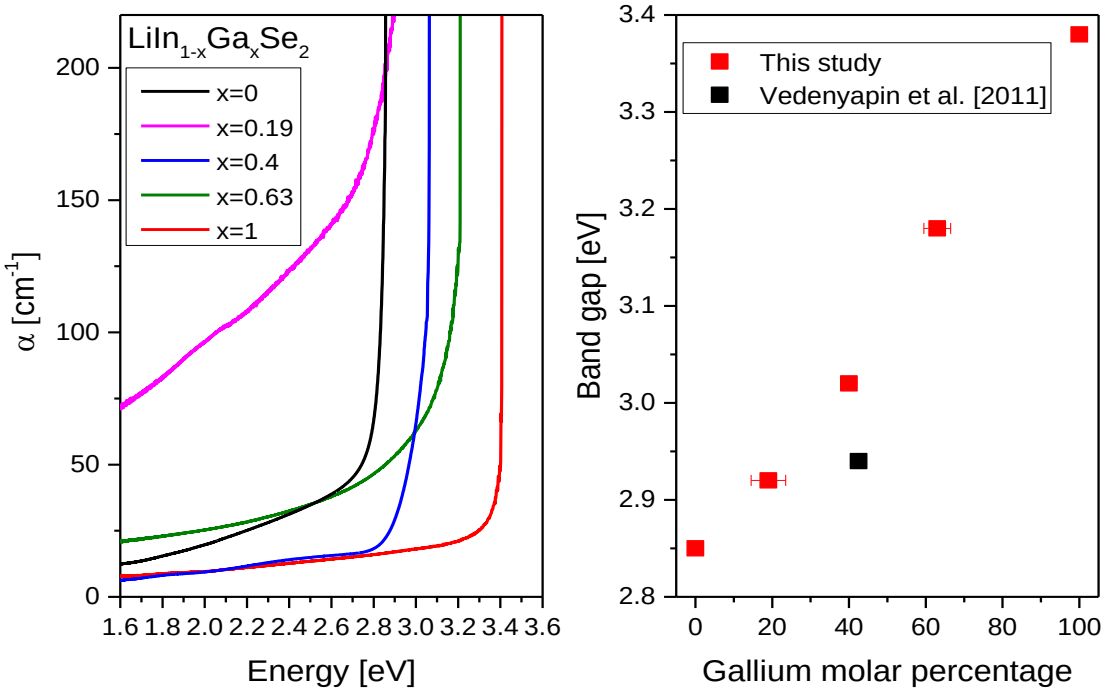

Figure 21 displays the room temperature absorption spectra for $LiIn_{1-x}Ga_xSe_2$ crystal on the left and the band gap trend for $LiIn_{1-x}Ga_xSe_2$ crystals on the right. The measured EDX composition, corresponding to each trace, is given in the legend. The room temperature band gap trend demonstrates a progressive increase as the gallium concentration is increased.

Conclusion

A set of mixed $LiIn_{1-x}Ga_xSe_2$ crystals have been synthesized and characterized. Moderately sized crystals of the $LiIn_{1-x}Ga_xSe_2$ system have been generated with the vertical Bridgman technique. This approach is viable to generate $LiIn_{1-x}Ga_xSe_2$ crystals, alter their lattice parameters and tune the optical properties of this system via the In/Ga ratio. The experimental results also suggest that the $LiIn_{0.6}Ga_{0.4}Se_2$ composition was the most stable intermediate in this study. Due to the tri-valent ionic radius mismatch, gallium segregation was observed; it is suggested that thermal gradient adjustments and post growth annealing can reduce the degree of segregation observed in growth yields. The presented evaluation shows promise for the generation of tunable lithium-containing chalcogenide solid-solutions.

REFERENCES

[1] Chadwick, J. (1932) Possible Existence of a Neutron. *Nature*, **129**, 312.

[2] Knoll, G.F. (2010*) Radiation detection and measurement.* New York, NY: John Wiley & Sons, Inc.

[3] Combes, C.M., Dorenbos, P., van Eijk, C.W.E., Krämer, K.W., & Güdel, H.U. (1999) Optical and scintillation properties of pure and Ce^{3+} -doped Cs_2LiYCl_6 and $Li_3YCl_6:Ce^{3+}$ crystals. *Journal of Luminescence*, **82**, 299-305.

[4] Iwanowska, J., Swiderski, L., Moszynski, M., Yanagida, T., Yokota, Y., Yoshikawa, A., Fukuda, K., Kawaguchi, N., Ishizu, S. (2011) Thermal neutron detection with Ce^{3+} doped $LiCaAlF_6$ single crystals. *Nuclear Instruments and Methods in Physics Research A,* **652**, 319-322.

[5] Kojima, T., Katagiri, M., Tsutsui, N., Imai, K., Matsubayashi, M., & Sakasai, K. (2004) Neutron scintillators with high detection efficiency. *Nuclear Instruments and Methods in Physics Research A*, **529**, 325-328.

[6] Unruh, T.C., Bellinger, S.L., Huddleston, D.E., McNeil, W.J., Patterson, E., Sobering, T.J., & McGregor, D.S. (2009) Design and operation of a 2-D thin-film semiconductor neutron detector array for use as a beamport monitor. *Nuclear Instruments and Methods in Physics Research A*, **605**, 150-153.

[7] McGregor, D.S., Lindsay, J.T., Brannon, C.C., & Olsen, R.W. (1996) Semi-Insulating Bulk GaAs as a Semiconductor Thermal-Neutron Imaging Device. *Nuclear Instruments and Methods in Physics Research A*, **380**, 271-275.

[8] McGregor, D.S., Vernon, S.M., Gersch, H.K., Markham, S.M., Wojtczuk, S.J., & Wehe, D.K. (2000) Self-Biased Boron-10 Coated High Purity Epitaxial GaAs Thermal Neutron Detectors. *IEEE Transaction on Nuclear Science,* **47**, 1364-1370.

[9] McGregor, D.S., Hammig, M.D., Gersch, H.K., Yang, Y-H., & Klann, R.T. (2003) Design Considerations for Thin Film Coated Semiconductor Thermal Neutron Detectors, Part 1: Basics Regarding Alpha Particle Emitting Neutron Reactive Films. *Nuclear Instruments and Methods A,* **500**, 272-308.

[10] Hohenberg, P. & Kohn, W. (1964) Inhomogeneous Electron Gas. *Phys. Rev. B*, **136**, 864-871.

[11] Kohn, W. & Sham, L. J. (1965) Self-Consistent Equations Including Exchange and Correlation Effects. *Phys. Rev. A*, **140**, 1133-1138.

[12] J.C. Phillips. (1958) Energy-Band Interpolation Scheme Based on a Pseudopotential. *Phys. Rev.*, **112**, 685.

[13] J.C. Phillips & L. Kleinman. (1959) New Method for Calculating Wave Functions in Crystals and Molecules. *Phys. Rev.*, **116**, 287.

[14] L. Kleinman & J.C. Phillips. (1960) Crystal Potential and Energy Bands of Semiconductors. III. Self-Consistent Calculations for Silicon. *Phys. Rev.*, **118**, 1153.

[15] Volker Heine. (1970) The Pseudopotential Concept. Solid *State Physics*, **24,** 1-36.

[16] Warren E. Pickett. (1989) Pseudopotential methods in condensed matter applications. *Computer Physics Reports*, **9**, 115-197.

[17] D. M. Ceperley & B. J. Alder. (1980) Ground State of the Electron Gas by a Stochastic Method. *Phys. Rev. Lett*., **45**, 566.

[18] J. P. Perdew,A. Zunger. (1981) Self-interaction correction to density-functional approximations for many-electron systems. *Phys. Rev. B*, **23**, 5048.

[19] A. D. Becke. (1988) Density-functional exchange-energy approximation with correct asymptotic behavior. *Phys. Rev. A*, **38**, 3098.

[20] J. P. Perdew, J. A. Chevary, S. H. Vosko, K. A. Jackson, M. R. Pederson, D. J. Singh, & C. Fiolhais. (1992) Atoms, molecules, solids, and surfaces: Applications of the generalized gradient approximation for exchange and correlation. *Phys. Rev. B,* **46**, 6671.

[21] J. P. Perdew, K. Burke, & M. Ernzerhof. (1996) Generalized Gradient Approximation Made Simple. *Phys. Rev. Lett.*, **77**, 3865.

[22] Kittel, C. (2005) *Introduction to Solid State Physics*. New York, NY: John Wiley & Sons, Inc.

[23] Callister, W.D. & Rethwisch, D.G. (2009) *Materials Science and Engineering: An Introduction*. New York, NY: John Wiley & Sons, Inc.

[24] Kouzes et al. (2010) Neutron detection alternatives to 3He for national security applications. *Nuclear Instruments and Methods in Physics Research Section A: Accelerators, Spectrometers, Detectors and Associated Equipment,* **623**, 1035-1045.

[25] D. Rezaei-Ochbelagh. (2012) Comparison of 3He and BF3 neutron detectors used to detect hydrogenous material buried in soil. *Radiation Physics and Chemistry,* **81**, 379-382.

[26] A.J Peurrung. (2000) Recent developments in neutron detection. *Nuclear Instruments and*

Methods in Physics Research Section A: Accelerators, Spectrometers, Detectors and Associated Equipment, **443**, 400-415.

[27] C.W.E van Eijk, A. Bessière & P. Dorenbos. Inorganic thermal-neutron scintillators. (2004) *Nuclear Instruments and Methods in Physics Research Section A: Accelerators, Spectrometers, Detectors and Associated Equipment,* **529**, 260-267.

[28] Albert G. Beyerle & Kenneth L. Hull. Neutron detection with mercuric iodide detectors. (1987) *Nuclear Instruments and Methods in Physics Research Section A: Accelerators, Spectrometers, Detectors and Associated Equipment,* **256**, 377-380.

[29] R. Hoppe. (1965) *Bull. Soc. Chim. Fr*., 1115.

[30] Isaenko, L.I. & Vasilyeva, I. G. (2008) Nonlinear $LiB^{III}C^{VI}_2$ crystals for mid-IR and far-IR: Novel aspects in crystal growth. *Journal of Crystal Growth,* **310**, 1954-1960.

[31] Isaenko, L., Vasilyeva, I., Merkulov, A., Yelisseyev, A., & Lobanov, S. (2005) Growth of new nonlinear crystals LiMX2 (M= Al, In, Ga; X=S, Se, Te) for the mid-IR optics. *Journal of Crystal Growth,* **275**, 217-223.

[32] Isaenko et al. (2006) Ternary Chalcogenides $LiBC_2$ (B=In, Ga; C=S, Se, Te) for mid-IR nonlinear optics. *Journal of Non-Crystalline Solids,* **352**, 2439-2443.

[33] Kamijoh, T. & Kuriyama, K. (1981) Single Crystal Growth and Characterization of $LiInSe_2$. *Journal of Crystal Growth,* **51**, 6-10.

[34] Vasilyeva, I. G., Nikolaev, R. E., Malakhov, V. V. & Isaenko, L. I. (2007) Effects of evaporation and melting on nonstoichiometry and inhomogeneity of $LiInSe_2$ crystals. *Journal of Thermal Analysis and Calorimetry,* **90**, 601-605.

[35] Weise, S & Krämer, V. (2003) Phase study of the system Li_2Se-In_2Se_3. *Journal of Thermal Analysis and Calorimetry,* **71**, 1035-1038.

[36] Panich, A.M., Yelisseyev, A.P., Lobanov, S.I., & Isaenko, L.I. (2004) Comparative Nuclear Magnetic Resonance Study of As-Grown and Annealed $LiInSe_2$ Ternary Compounds. *Hyperfine Interactions*, **159**, 199-203.

[37] Isaenko, L., Yelisseyev, A., & Lobanov, S. (2002). $LiInSe_2$: A biaxial chalcogenide crystal for nonlinear optical applications in the midinfrared. *Journal of Applied Physics*, **91**, 9475-9480.

[38] Brenden Wiggins, Eugene, Tupitsyn, Pijush Bhattacharya, Emmanuel Rowe, Eric Lukosi, Ondrej Chvala, Arnold Burger, Ashley Stowe. (2013) Investigation of non-uniformity and inclusions in ^{6}LiInSe2 utilizing laser induced breakdown spectroscopy (LIBS). Proc. SPIE **8852**, 88520M.

[39] Petrov et al. (2010) Optical, thermal, electrical, damage, and phase-matching properties of lithium selenoindate. *J. Opt. Soc. Am. B,* **27**, 1902–1927.

[40] Cui et al. (2013) Defects in 6LiInSe2 neutron detector investigated by photo-induced current transient spectroscopy and photoluminescence. *Applied Physics Letters*, **103**, 092104

[41] Tupitsyn et al. (2014) Lithium containing chalcogenide single crystals for neutron detection. *Journal of Crystal Growth*, **393**, 23-27.

[42] Pankove, J.I. (1971) *Optical Processes in Semiconductors*. Englewood Cliffs, New Jersey: Prentice-Hall, Inc.

[43] P. Dorenbos, J.T.M. De Haas & C.W.E. Van Eijk. (1995) Non-proportional response of scintillation crystals to X-rays and γ-rays. *Radiation Measurements*, **24**, 355-358.

[44] Pieter Dorenbos. Light output and energy resolution of Ce3+-doped scintillators. (2002) *Nuclear Instruments and Methods in Physics Research Section A: Accelerators, Spectrometers, Detectors and Associated Equipment*, **486**, 208-213.

[45] Alan Owens & A. Peacock. (2004) Compound semiconductor radiation detectors. *Nuclear Instruments and Methods in Physics Research Section A: Accelerators, Spectrometers, Detectors and Associated Equipment,* **531**, 18-37.

[46] Qi Li, Joel Q. Grim, R.T. Williams, G.A. Bizarri, W.W. Moses. (2011) The role of hole mobility in scintillator proportionality. *Nuclear Instruments and Methods in Physics Research Section A: Accelerators, Spectrometers, Detectors and Associated Equipment,* **652**, 288-291.

[47] Tupitsyn et al. (2012) Single crystal of LiInSe2 semiconductor for neutron detector. *Applied Physics Letters,* **101**, 202101

[48] National Nuclear Data Center. Thermal Neutron Capture γ's (CapGam). http://www.nndc.bnl.gov/capgam/.

[49] Vega-Carrillo, H.R., Manzanares-Acuna, E., Becerra-Ferreiro, A.M. & Carrillo-Nunez, A. (2002) Neutron and gamma-ray spectra of ^{239}PuBe and ^{241}AmBe. *Applied Radiation and Isotopes,* **57**, 167-170.

[50] N. D'Olympia et al. (2013) Pulse-shape analysis of CLYC for thermal neutrons, fast neutrons, and gamma-rays. *Nuclear Instruments and Methods in Physics Research Section A: Accelerators, Spectrometers, Detectors and Associated Equipment,* **714**, 121-127.

[51] www.crystals.saint-gobain.com/BGO_Scintillator.aspx

[52] I.G. Vasilyeva, A.A. Pochtar, L.I. Isaenko. (2014) Origin of the solid solution in the LiInSe2–In2Se3 system. *Journal of Solid State Chemistry*, **220**, 91-96.

[53] L. Isaenko, A. Yelisseyev, S. Lobanov, A.Titov, V. Petrov, J.-J. Zondy, P. Krinitsin, A. Merkulov, V. Vedenyapin, J. Smirnova. (2003) *Cryst. Res. Technol*, **38**, 379–387.

[54] K. Takeya, Y. Takemoto, I. Kawayama, H. Murakami, T. Matsukawa, M. Yoshimura, Y. Mori, M. Tonouchi. (2010) Terahertz emission from coherent phonons in lithium ternary

chalcopyrite crystals illuminated by 1560 nm femtosecond laser pulses. *Europhysics Letters*, **91**, 2.

[55] Q. Liang, S. Wang, X. Tao, T. Dekorsy. (2014) Optical properties of $LiInSe_2$ in the THz frequency regime. *Opt. Mater. Express,* **4**, 1336–1344.

[56] Y. Li, W. Fan, H. Sun, X. Cheng, P.Li, X.Zhao. (2011) Computational insight into the effect of monovalent cations on the electronic, optical, and lattice dynamic properties of $XInSe_2$ (X=Cu, Ag, Li). *Journal of Applied Physics*, **109**, 113535

[57] A. C. Stowe, J. Woodward, E. Tupitsyn, E. Rowe, B. Wiggins, L. Matei, P. Bhattacharya, A. Burger. (2013) Crystal growth in $LiGaSe_2$ for semiconductor radiation detection applications. *Journal of Crystal Growth,* **379**, 111–114.

[58] V. Vedenyapin, L. Isaenko, A. Yelisseyev, S. Lobanov, A. Tyazhev, G. Marchev, V. Petrov. (2011) New mixed $LiGa_{0.5}In_{0.5}Se_2$ nonlinear crystal for the mid-IR. Proc. SPIE **7917**, 79171L.

[59] B. Wiggins, J. Bell, A. Burger, K. Stassun, A. C. Stowe. (2015) Investigations of $^6LiIn_{1-x}Ga_xSe_2$ semi-insulating crystals for neutron detection. Proc. of SPIE **9593**, 95930B.

[60] A. Ben Fredj, M. Debbichi, M. Said. (2007) Influence of the composition fluctuation and the disorder on the bowing band gap in semiconductor materials. *Microelectronics Journal*, **38**, 860–870.

[61] A. V. Gektin, A. N. Belsky, A. N. Vasil'ev. (2014) Scintillation Efficiency Improvement by Mixed Crystal Use. *IEEE Transactions on Nuclear Science*, **61**, 262–270.

[62] B. Wiggins, M. Groza, E. Tupitsyn, E. Lukosi, K. Stassun, A. Burger, and A. C. Stowe. (2015) Scintillation properties of semiconducting $^6LiInSe_2$ crystals to ionizing radiation. *Nuclear Instruments and Methods in Physics Research A*, **801**, 73–77.

[63] L.-H. Li, J.-Q. Li, L.-M. Wu. (2008) Electronic structures and optical properties of wurtzite type LiBSe2 (B=Al, Ga, In): A first-principles study. *Journal of Solid State Chemistry*, **181**, 2462–2468.

[64] T. Ma, L. Sun, C. Xu, Y. Chen. (2011) First principles study of lattice dynamics and thermodynamic properties of LiInX2 (X=S,Se,Te). *Journal of Alloys and Compounds*, **509**, 9733–9741.

[65] B. Lagoun, T. Bentria, B. Bentria. (2013) Ab initio investigation of the elastic and piezoelectric properties of lithium based Chalcogenides $LiMX_2$ (M=Ga, In; X=S, Se). *Computational Materials Science*, **68**, 379–383.

[66] G. Kresse,J. Hafner, (1993) Ab initio molecular dynamics for liquid metals. *Phys. Rev. B*, **47**, 558.

[67] G. Kresse,J. Joubert, (1999) From ultrasoft pseudopotentials to the projector augmented wave method. *Phys. Rev. B*, **59**, 1758.

[68] M. Gajdoš, K. Hummer, G. Kresse, J. Furthmüller, & F. Bechstedt. (2006) Linear optical properties in the projector-augmented wave methodology. *Phys. Rev. B*, **73**, 045112.

[69] K. Momma,F. Izumi, J. Appl. Crystallogr. (2011) VESTA 3 for three-dimensional visualization of crystal, volumetric and morphology data. *Journal of Applied Crystallography*, **44**, 1272–1276.

[70] W. Hönle, G. Kühn, H. Neumann, Z. (1986) The crystal structure of $LiInSe_2$. *Anorg. Allg. Chem.*, **543**, 161-168.

[71] E. Tupitsyn, P. Bhattacharya, E. Rowe, L. Matei, M. Groza, B. Wiggins, A. Burger, A. Stowe. (2012) Single crystal of $LiInSe_2$ semiconductor for neutron detector. *Applied Physics Letters*, **101**, 202101

[72] T. Kamijoh, T. Nozaki, K. Kuriyama, J. (1982) Dielectric constants and bond parameters of $LiInSe_2$ and $LiGaSe_2$. *Journal of Applied Physics*, **53**, 761–763.

[73] Stowe, A. C. & Burger, A. (2014) Methods for synthesizing semiconductor quality chalcopyrite crystals for nonlinear optical and radiation detection applications and the like. US Patent Application US 20140144373 A1

[74] Zane W. Bell, A. Burger, Liviu Matei, Michael Groza, Ashley Stowe, Joshua Tower, Alireza Kargar, Huicong Hong. (2015) Neutron detection with $LiInSe_2$. Proc. SPIE **9593**, 95930D.

[75] Yu.M. Andreev, V.V. Atuchin, G.V. Lanskii, N.V. Pervukhina, V.V. Popov, N.C. Trocenco. (2005) Linear optical properties of $LiIn(S_{1-x}Se_x)_2$ crystals and tuning of phase matching conditions. *Solid State Sciences*, **7**, 1188-1193.

[76] M.B. Chadwick, M. Herman, P. Oblo.žinský, M.E. Dunn, Y. Danon, A.C. Kahler, D.L. Smith, B. Pritychenko, G. Arbanas, R. Arcilla, R. Brewer, D.A. Brown, R. Capote, A.D. Carlson, Y.S. Cho, H. Derrien, K. Guber, G.M. Hale, S. Hoblit, S. Holloway, T.D. Johnson, T. Kawano, B.C. Kiedrowski, H. Kim, S. Kunieda, N.M. Larson, L. Leal, J.P. Lestone, R.C. Little, E.A. McCutchan, R.E. MacFarlane, M. MacInnes, C.M. Mattoon, R.D. McKnight, S.F. Mughabghab, G.P.A. Nobre, G. Palmiotti, A. Palumbo, M.T. Pigni, V.G. Pronyaev, R.O. Sayer, A.A. Sonzogni, N.C. Summers, P. Talou, I.J. Thompson, A. Trkov, R.L. Vogt, S.C. van der Marck, A. Wallner, M.C. White, D. Wiarda, P.G. Young. (2011) ENDF/B-VII.1: Nuclear Data for Science and Technology: Cross Sections, Covariances, Fission Product Yields and Decay Data. *Nucl. Data Sheets*, **112**, 2987-2996.

[77] A.C. Larson & R.B. Von Dreele. (2000) General Structure Analysis System (GSAS). Los

Alamos National Laboratory Report LAUR 86-748.

[78] B.H. Toby. (2001) EXPGUI, a graphical user interface for GSAS. *Journal of Applied Crystallography*, **34**, 210-213.

[79] K. Kuriyama & T. Kozaki. (1981) Single-crystal growth and characterization of LiGaSe2, *Journal of Applied Physics*, **52**, 6441-6443.